

This is an Open Access article, distributed under the terms of the Creative Commons Attribution licence (<http://creativecommons.org/licenses/by/4.0/>), which permits unrestricted re-use, distribution, and reproduction in any medium, provided the original work is properly cited.

doi:10.1017/jfm.2019.29

Condensates in thin-layer turbulence

Adrian van Kan^{1,2,†} and Alexandros Alexakis²

¹Fakultät für Physik und Astronomie, Universität Heidelberg, Im Neuenheimer Feld 226, D-69120 Heidelberg, Germany

²Laboratoire de Physique de l'École normale supérieure, ENS, Université PSL, CNRS, Sorbonne Université, Université Paris-Diderot, Sorbonne Paris Cité, 75005 Paris, France

(Received 1 August 2018; revised 25 October 2018; accepted 26 December 2018)

We examine the steady state of turbulent flows in thin layers using direct numerical simulations. It is shown that when the layer thickness is smaller than a critical height, an inverse cascade arises which leads to the formation of a steady state condensate where most of the energy is concentrated in the largest scale of the system. For layers of thickness smaller than a second critical height, the flow at steady state becomes exactly two-dimensional. The amplitude of the condensate is studied as a function of layer thickness and Reynolds number. Bi-stability and intermittent bursts are found close to the two critical points. The results are interpreted based on a mean-field three-scale model that reproduces some of the basic features of the numerical results.

Key words: low-dimensional models

1. Introduction

Turbulent flows in geophysical and astrophysical contexts are often subject to geometrical constraints, such as thinness in a particular direction, that can strongly affect the behaviour of the flow. This occurs, for instance, in planetary atmospheres and oceans (Pedlosky 2013) whose behaviour can strongly deviate from the classical three-dimensional homogeneous and isotropic turbulence. This is related to the well-known fact that the behaviour of flows at large Reynolds numbers Re depends on the dimensionality of the system. In three dimensions, vortex stretching transfers energy to small scales in a direct cascade (Frisch 1995). By contrast, in two dimensions, the conservation of enstrophy in addition to energy gives rise to an inverse energy cascade, a transfer of energy to the large scales (Boffetta & Ecke 2012). Flows in thin layers display properties of both systems, with the large scales behaving like a two-dimensional (2-D) flow and the small scales behaving like a 3-D flow. As a result, such systems are known to cascade energy both to large and to small scales (Smith, Chasnov & Waleffe 1996). In fact, it has been shown in (Celani, Musacchio & Vincenzi 2010; Benavides & Alexakis 2017; Musacchio & Boffetta 2017) that as the height of the layer H is varied, the system transitions from a state where energy cascades only to the small scales for large H , to a state where energy cascades to both large and small scales when H is smaller than approximately

† Email address for correspondence: avankan@lps.ens.fr

half the size of the forcing length scale ℓ . In particular Benavides & Alexakis (2017), using a Galerkin truncated model of the full Navier–Stokes equations, were able to provide strong evidence of the criticality of the transition. In addition, they observed a second transition to exact two-dimensionalisation for layers of very small thickness $H \propto \ell Re^{-1/2}$. This transition had been predicted theoretically using bounding techniques by Gallet & Doering (2015). Similar transitions from a strictly forward cascade to an inverse cascade have been observed in other systems like rotating turbulence (Deusebio *et al.* 2014), stratified turbulence (Sozza *et al.* 2015), rotating and stratified flows (Marino, Pouquet & Rosenberg 2015), magneto-hydrodynamic systems (Alexakis 2011; Seshasayanan, Benavides & Alexakis 2014; Seshasayanan & Alexakis 2016) and helically constrained flows (Sahoo & Biferale 2015; Sahoo, Alexakis & Biferale 2017), to mention a few (see Alexakis & Biferale (2018) for a review).

The thin layer, however, remains possibly the simplest model exhibiting such transitions and it thus deserves a detailed study at the different stages of inverse cascade evolution. In the presence of an inverse cascade, for finite systems and in the absence of a large-scale dissipation term, there are two stages in the development of the flow. In the first stage (at early times), energy is transferred to larger and larger scales by the inverse cascade. This process stops, however, when scales comparable to the system size are reached, after which energy starts to pile up at these largest scales. In the long-time limit, the increase of the large-scale energy saturates and a condensate is formed, where nearly all energy is found in the first few Fourier modes. For 2-D Navier–Stokes turbulence, the possibility of such a condensation phenomenon was first conjectured in the seminal paper of Kraichnan (1967), first seen in direct numerical simulations by Hossain, Matthaeus & Montgomery (1983), further explored quantitatively by Smith & Yakhot (1993, 1994) and, more recently, by Chertkov *et al.* (2007), Bouchet & Simonnet (2009), Chan, Mitra & Brandenburg (2012), Frishman, Laurie & Falkovich (2017), Frishman & Herbert (2018). Spectral condensation has also been studied in other quasi-2-D systems such as quasi-geostrophic flows (see Vallis & Maltrud 1993; Kukharkin, Orszag & Yakhot 1995; Kukharkin & Orszag 1996; Venaille & Bouchet 2011). In terms of the real space flow field, this spectral condensation corresponds to coherent system-size vortices or shear layers. In two dimensions, where the cascade of energy is strictly inverse, a steady state in the condensate regime is realised when the energy of the condensate is so large that the dissipation due to viscosity at large scales balances the energy injection due to the forcing. For split cascading systems, this is not necessarily true due to the presence of non-vanishing 3-D flow variations associated with the direct cascade. Therefore, in this case other processes exist that can redirect the energy back to the small scales where viscous dissipation is more efficient. Such mechanisms have been demonstrated for rotating turbulence, where a flux-loop mechanism has been identified (cf. Bartello, Métais & Lesieur 1994; Alexakis 2015; Seshasayanan & Alexakis 2018). Similar condensates have also been observed in 3-D fast rotating convection (Favier, Silvers & Proctor 2014; Guervilly, Hughes & Jones 2014; Rubio *et al.* 2014; Favier, Guervilly & Knobloch 2019).

Condensates in thin layers have been observed experimentally: the first study by Sommeria (1986) was followed by the important contributions of Paret & Tabeling (1997, 1998) and more recently by Shats, Xia & Punzmann (2005), Shats *et al.* (2007), Xia *et al.* (2008), Xia, Shats & Falkovich (2009), Byrne, Xia & Shats (2011), Xia *et al.* (2011). An up-to-date review of relevant experiments is presented in Xia & Francois (2017). These experiments operate primarily in the long-time limit in which the condensate is fully developed. This wealth of experimental studies of thin-layer

condensates is in striking contrast with the existing numerical results which have focused exclusively on the transient growth of total kinetic energy due to the inverse cascade. In these numerical simulations, the condensate state reached after long time in the thin-layer case has not yet been examined due to the long computation time needed. In this study, we aim to fill this gap and investigate the behaviour of turbulent flow at the condensate stage for a thin layer forced at intermediate scales, using direct numerical simulations (DNS) and low-order modelling. The DNS provide a detailed picture of the behaviour of the full system, while the modelling shines light on the main physical processes involved in the problem.

The remainder of this article is structured as follows. In §2, we present the set-up and define the quantities we will be measuring. In §3, we present the results of a large number of direct numerical simulations (DNS) of thin-layer turbulence. Next, in §4, we discuss the behaviour close to the two critical points and in §5, we present spectra and spectral fluxes of energy. In §6, we introduce a low-order model which captures many features of the DNS results. Finally, in §7, we discuss our results and summarise.

2. Physical set-up

In this section, we describe the set-up to be investigated. We consider the idealised case of forced incompressible three-dimensional flow in a triply periodic box of dimensions $L \times L \times H$. The thin direction H will be referred to as the vertical ‘z’ direction and the remaining two as the horizontal ‘x’ and ‘y’ directions. The geometry of the domain is illustrated in figure 1. The flow obeys the incompressible Navier–Stokes equation:

$$\partial_t \mathbf{u} + \mathbf{u} \cdot \nabla \mathbf{u} = -\nabla P + \nu \nabla^2 \mathbf{u} + \mathbf{f}, \quad (2.1a)$$

$$\nabla \cdot \mathbf{u} = 0, \quad (2.1b)$$

where \mathbf{u} is the velocity field, P is physical pressure divided by constant density and ν is (kinematic) viscosity. Energy is injected into the system by \mathbf{f} , a stochastic force, that depends only on x and y and has only x and y components, i.e. that is a two-dimensional–two-component (2D2C) field. We make this assumption firstly to specifically force the inversely cascading components of the flow and secondly because it is widely used in previous studies such as Smith *et al.* (1996), Celani *et al.* (2010), Deusebio *et al.* (2014), Gallet & Doering (2015) and thus enables us to compare more easily with the literature. The force is divergence free, hence it can be written as $\mathbf{f} = (-\partial_y \psi, \partial_x \psi, 0)$. The spectrum of \mathbf{f} is concentrated in a ring of wavenumbers of radius $k_f \equiv 2\pi/\ell$. It is delta correlated in time, which leads to a fixed mean injection of energy $\langle \mathbf{u} \cdot \mathbf{f} \rangle = \epsilon$, where $\langle \cdot \rangle$ denotes an ensemble average over infinitely many realisations. We use random initial conditions whose small energy is spread out over a range of wavenumbers. In some cases, in order to compare with previous studies, we used a hyper-viscosity, which amounts to replacing $\nu \nabla^2 \mathbf{u}$ by $-\nu_n (-\nabla^2)^n \mathbf{u}$.

The system (2.1b) is characterised by three non-dimensional parameters: the Reynolds number based on the energy injection rate $Re = (\epsilon \ell^4)^{1/3}/\nu$, the ratio between forcing scale and domain height $Q = \ell/H$ and the ratio between forcing scale and the horizontal domain size $K = \ell/L$. The ratio between K and Q gives the aspect ratio $A = K/Q = H/L$ of the domain. The Kolmogorov dissipation length is denoted as $\eta = \nu^{3/4}/\epsilon^{1/4} = \ell Re^{3/4}$.

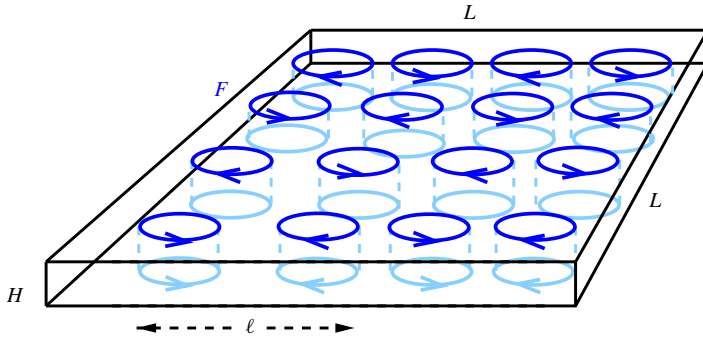


FIGURE 1. (Colour online) The domain used is a box of height H and square base of side length L . The forcing is invariant along the thin direction and stochastic with fixed mean rate of energy input, while involving only wavenumbers \mathbf{k} with $|\mathbf{k}| = k_f = 2\pi/\ell$. The thin direction will be referred to as the vertical, the others as the horizontal directions.

Re	203	305	406	609	870	2031	4062	Hyper
$1/K$	8	8 and 16	8	8	8	8	8	8
$n_x = n_y$	256	256 and 512	256	512	512	1024	2048	1024
n_z	16	16	16	32	32	64	128	64
# runs	40	40	40	30	30	10	2	4

TABLE 1. Summary of the different runs performed. For each Re and K several runs for different values of Q have been performed. The horizontal resolution is n_x, n_y , while n_z stands for the vertical resolution at $Q = 2$. The vertical resolution was changed with Q to maintain an isotropic grid, $Kn_x = Kn_y = Qn_z$ wherever possible.

The simulations performed for this work used an adapted version of the Geophysical High-Order Suite for Turbulence (GHOST) which uses pseudo-spectral methods including $2/3$ aliasing to solve for the flow in the triply periodic domain, (see Mininni *et al.* 2011). The resolution was varied from $256^2 \times 16$ grid points to $2048^2 \times 128$ grid points depending on the values of the parameters. To explore the space spanned by these three parameters, we have performed systematic numerical experiments: for a fixed value of Re and $K = 1/8$, different simulations are performed with Q varying from small to large values. The runs are continued until a steady state is reached where all quantities fluctuate around their mean value. This is repeated for eight different values of Re from $Re = 203$ (resolution $256^2 \times 16$) to 4062 (resolution $2048^2 \times 128$) and for one value of hyper-viscosity ($n = 8, \nu_8 = 10^{-38}$ as in (Celani *et al.* 2010)), as a consistency check, since many of the previous studies of thin-layer turbulence used hyper-viscosity. For $Re = 305$, we also perform a run with $K = 1/16$ ($L \rightarrow 2L$). The number of runs performed for each Re are summarised in table 1.

To quantify the energy distribution among different scales it is convenient to work in Fourier space. The Fourier series expansion of the velocity reads

$$\mathbf{u}(\mathbf{x}, t) = \sum_{\mathbf{k}} \hat{\mathbf{u}}_{\mathbf{k}} e^{i\mathbf{k}\cdot\mathbf{x}}, \quad \hat{\mathbf{u}}_{\mathbf{k}} = \frac{1}{L^2 H} \int \mathbf{u}(\mathbf{x}, t) e^{-i\mathbf{k}\cdot\mathbf{x}} d\mathbf{x} \quad (2.2a,b)$$

where $\hat{\mathbf{u}}_k = (\hat{u}_k^{(x)}, \hat{u}_k^{(y)}, \hat{u}_k^{(z)})$ and the sum runs over all $\mathbf{k} \in ((2\pi/L)\mathbb{Z})^2 \times (2\pi/H)\mathbb{Z}$. In the pseudo-spectral calculations, this sum is truncated at a finite k_{res} . Since flow in a thin layer is a highly anisotropic system, it is important to consider quantities in the vertical and horizontal directions separately. For this purpose, we monitor various quantities in our simulations: first of all, the total energy spectrum as a function of horizontal wavenumber

$$E_{tot}(k_h) = \frac{1}{2} \sum_{\substack{k \\ k_x^2 + k_y^2 = k_h^2}} |\hat{\mathbf{u}}_k|^2. \quad (2.3)$$

In addition, we monitor different components of domain-integrated energy, namely the total horizontal kinetic energy

$$\frac{1}{2} U_h^2 = \frac{1}{2} \sum_k (|\hat{u}_k^{(x)}|^2 + |\hat{u}_k^{(y)}|^2) \quad (2.4)$$

(based on the (vertically averaged) 2D2C field only), the large-scale horizontal kinetic energy

$$\frac{1}{2} U_{ls}^2 = \frac{1}{2} \sum_{\substack{k \\ k < k_{max} \\ k_z = 0}} (|\hat{u}_k^{(x)}|^2 + |\hat{u}_k^{(y)}|^2), \quad (2.5)$$

where $k_{max} = \sqrt{22}\pi/L$, as well as the (vertically averaged) large-scale kinetic energy in the z component

$$\frac{1}{2} U_z^2 = \frac{1}{2} \sum_{\substack{k \\ k < k_{max} \\ k_z = 0}} |\hat{u}_k^{(z)}|^2 \quad (2.6)$$

and the three-dimensional kinetic energy (3-D energy), defined as

$$\frac{1}{2} U_{3D}^2 = \frac{1}{2} \sum_{\substack{k \\ k_z \neq 0}} |\hat{\mathbf{u}}_k|^2. \quad (2.7)$$

3. Results from the direct numerical simulations

In this section, we present the results obtained from our simulations. For a given set of parameters Re , Q , K , two different behaviours are possible. For thick layers $Q \ll 1$, 3-D turbulence is observed, i.e. there is no inverse cascade and the energy injected by the forcing is transferred to the small scales where it is dissipated. No system-size structures appear in this case. For thin layers $Q \gg 1$, a split cascade is present with part of the energy cascading inversely to the large scales and part of the energy cascading forward to the small scales. For these layers, at steady state, coherent system-size vortices appear with very large amplitudes.

A visualisation of the flow field in these two different states is shown in figure 2 for the 3-D turbulence and condensate states. Typical time series of U_h^2 for a thick layer (forward cascade) and a thin layer (inverse cascade) are shown in figure 3(a). For the thick layer, the total energy fluctuates around a mean value of order $(\epsilon\ell)^{2/3}$, while for the thin layer, the energy saturates to a much larger value. The energy spectra for the two runs of figure 3(a) at the steady state are shown in figure 3(b), showing quantitatively that energy is concentrated in the large scales for the two

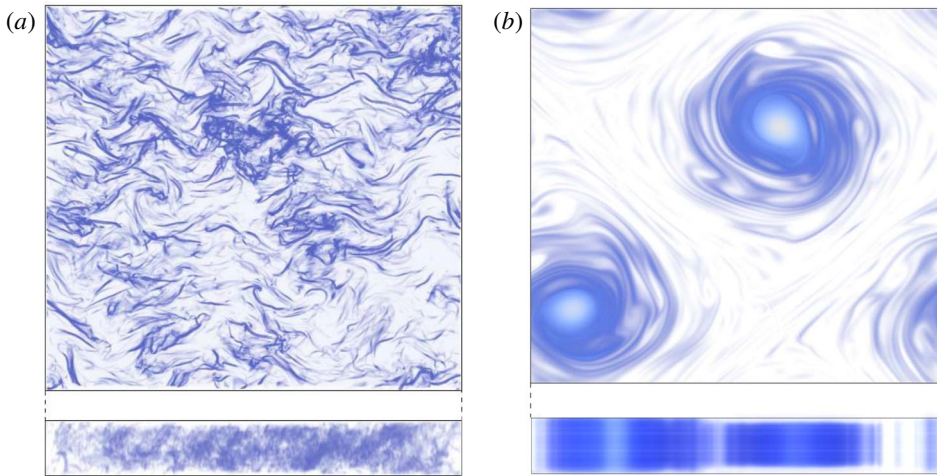


FIGURE 2. (Colour online) Typical flow fields in the steady state of 3-D turbulence (a) and 2-D turbulence (b) regimes, visualised using squared vorticity. The boxes below show the corresponding side views. Note the astonishing similarity between this figure and figure 1(a,b) of the experimental study by Xia *et al.* (2011).

different cases. In more detail, U_h^2 for the thin layer shows two different stages: first, at early times, there is a linear increase with time and second, there is saturation at late times. Therefore, to fully describe the evolution of the system, we need to quantify the rate of the initial energy increase and the energy at which it saturates. The red-dashed line indicates a fit to the initial linear increase. This slope provides a measurement of the rate ϵ_{inv} at which energy cascades inversely. For the steady state stage, the black dashed-dot line indicates the mean value at late times. For all runs, we measure the slope of the U_h^2 curve and the steady state mean values of all corresponding energies defined in the previous section. For the runs of high resolution, to accelerate convergence, the large-scale velocity $\mathbf{u}_{k=1}$ (from a run at the early stage) was increased artificially and the run continued. Alternatively, an output of a converged run was used as initial condition. However, all cases were run sufficiently long to demonstrate that they have reached a steady state.

Figure 4 shows the slopes of the initial total energy increase ϵ_{inv} , measured as illustrated in figure 3(a) for all our numerical simulations. The slopes are non-dimensionalised by the energy input rate ϵ and plotted versus Q for all different values of Re including the hyper-viscous runs. The slope at this early stage measures the strength of inverse energy transfer. At small Q (deep layers), the slope vanishes for all runs, showing that no inverse cascade is present. Moving to larger Q , for every Re , there is a critical value $Q_{3D}(Re)$ of Q above which the slope becomes non-zero. This is the birth of the inverse cascade. Figure 5 shows estimates of Q_{3D} as a function of Re : the upper curve shows the smallest Q for which an inverse cascade was observed for that given Re while the lower curve shows the largest Q for which no inverse cascade was observed. The critical value Q_{3D} lies between these two curves. The point Q_{3D} shifts to larger Q as Re is increased but eventually for the two largest Re simulated, namely $Re = 2031$ and $Re = 4062$, as well as the hyper-viscous run, Q_{3D} saturates at $Q_{3D} \approx 2.5$. (Previous findings (Celani *et al.* 2010) estimated this value to $Q_{3D} \approx 2$, however in that work too limited a range of values of Q was

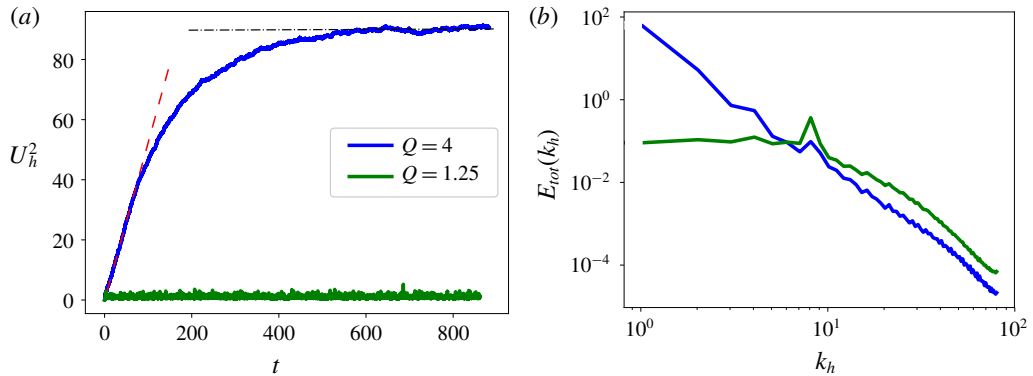


FIGURE 3. (Colour online) (a) Shows the typical time evolution of U_h^2 for $Q = 1.25 < Q_{3D}$ and $Q = 4 > Q_{3D}$. In the former case, U_h^2 remains small. In the latter, there is an initially linear increase whose slope measures the rate of inverse energy transfer. After long time, U_h^2 reaches its steady state value. Two quantities are measured: the initial slope (red-dashed line) and the condensate value (horizontal black dashed-dot line). A similar evolution observed in an experiment is shown in Xia *et al.* (2009) figure 6. (b) Shows the corresponding spectra: in the presence of an inverse cascade there is a maximum at the largest scale, while in its absence the maximum is near the forcing scale.

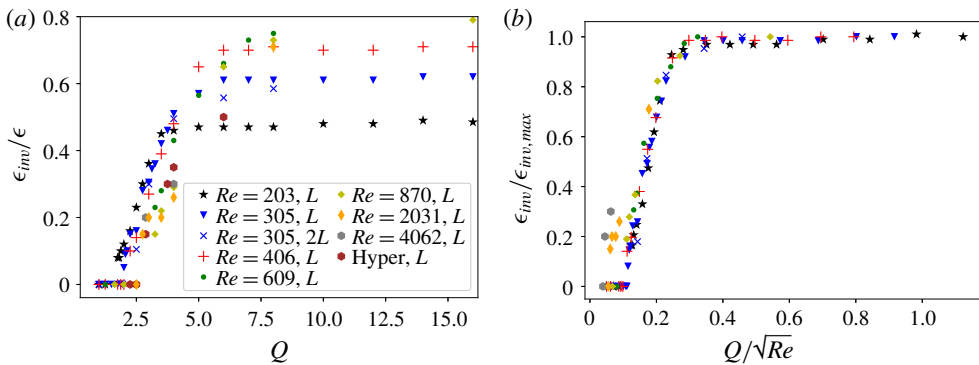


FIGURE 4. (Colour online) (a) Initial slopes, measured as indicated in figure 3(a), non-dimensionalised by the energy injection rate ϵ , as a function of Q ($\propto 1/H$) for all Re used. The same symbols are used in all plots in this section. Thick layers are at small Q (left) and thin layers at large Q (right). (b) The same data collapsed by a rescaling of the abscissa by \sqrt{Re} and the coordinate by the maximum value obtained for that Reynolds number.

used to be able to precisely pinpoint Q_{3D} . Another possible reason for the different result is the different value of $1/K$ associated with the different forcing wavenumber $k_f = 16$ used). The saturation of $Q_{3D} \approx 2.5$ indicates that Q_{3D} converges to this value at large Re . For $Q > Q_{3D}$, the slope begins increasing linearly $\epsilon_{inv} \propto Q - Q_{3D}$. (We note that small slopes are hard to distinguish from zero slope since the difference only becomes apparent after a long simulation time.)

If Q is increased further, a point Q_{2D} is reached beyond which the slope becomes independent of Q . Above this second critical point, the flow becomes exactly two-

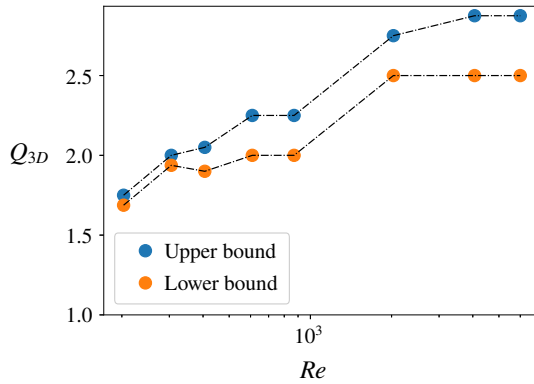


FIGURE 5. (Colour online) Estimated value of Q_{3D} as a function of Re . The top line shows the smallest value of Q for which an inverse cascade was observed and the bottom line shows the largest value of Q for which no inverse cascade was observed. The rightmost point indicates the results from the hyper-viscous runs.

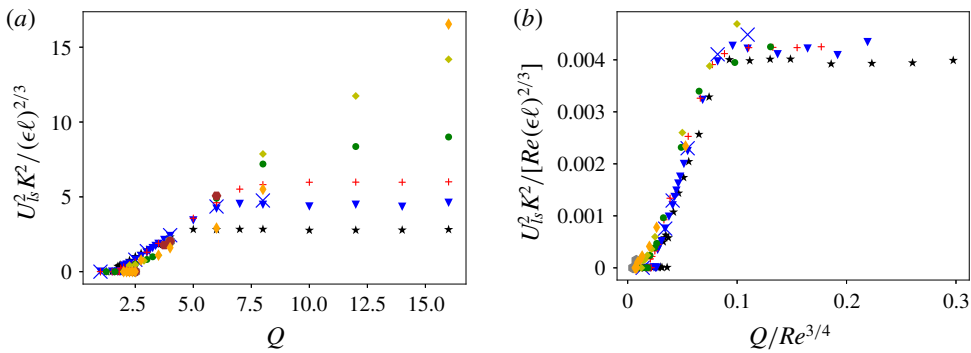


FIGURE 6. (Colour online) (a) U_{ls}^2 as defined in equation (2.5), non-dimensionalised by $(\epsilon \ell)^{2/3}/K^2$ as a function of Q . (b) The same data (excluding hyper-viscous run), with large-scale energy rescaled by $1/Re$ and plotted versus $Q/Re^{3/4}$ showing a satisfactory data collapse. The value $Q_{3D}/Re^{3/4}$ (where U_{ls}^2 plateaus) coincides for all Re at $Q/Re^{3/4} \approx 0.09-0.1$.

dimensional (Benavides & Alexakis 2017). The value of Q_{2D} increases with Re as $Q_{2D} \propto Re^{1/2}$. This scaling is verified in this work as well and shown in figure 4(b). The two critical points Q_{3D} and Q_{2D} at this early stage of development of the inverse cascade have been studied in detail in the past (Celani *et al.* 2010; Benavides & Alexakis 2017).

Here we mostly focus on the second stage of evolution: the steady state and the properties of the condensate. Figure 6 shows the equilibrium value of U_{ls}^2 , as defined in equation (2.5), non-dimensionalised by the forcing energy scale $(\epsilon \ell)^{2/3}$ and multiplied by K^2 . In the left panel, it is plotted versus Q (figure 6a) and in the right panel it is rescaled by $1/Re$ and plotted versus $\eta/H = QRe^{-3/4}$ (figure 6b). First consider figure 6(a). At small Q , there is very little energy in the large scales. This corresponds to the values of Q that displayed no inverse cascade at the initial stage. In the absence of an inverse cascade, the large scales only possess a small non-zero

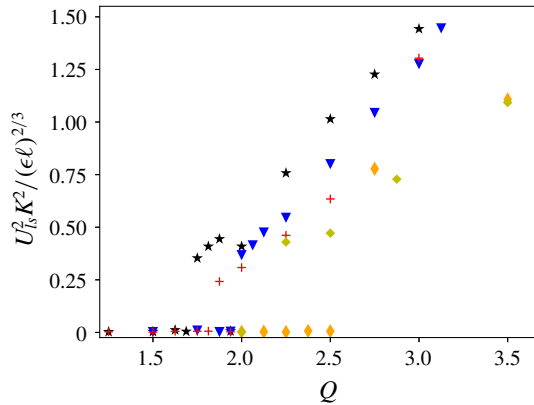


FIGURE 7. (Colour online) Zoomed-in version of figure 6(a) showing that there is a discontinuity in $U_{ls}^2/(\epsilon\ell)^{2/3}$ at Q_{3D} for all Reynolds numbers up to the second highest simulated.

energy and are expected to be in a thermal equilibrium state (Kraichnan 1973; Dallas, Fauve & Alexakis 2015; Cameron, Alexakis & Brachet 2017). For $Q > Q_{3D}$ the energy in the large scale takes larger values. In all cases, the energy increases nearly linearly $U_{ls}^2 \propto (Q - Q_{3D})$ for $Q_{2D} > Q > Q_{3D}$. With the chosen coordinate, the close coincidence of the experiments with $K = 1/8$ and $K = 1/16$ at $Re = 305$ indicates a scaling of $U_{ls}^2 \propto L^2$. If we zoom in on Q_{3D} (see figure 7), we observe clear signs of small but discontinuous jumps of U_{ls}^2 at Q_{3D} that are not visible in the zoomed out figure 6(a). These cases are examined in more detail in the next section.

The increase of the large-scale energy stops at the second critical point Q_{2D} , where U_{ls}^2 becomes independent of Q . It is noteworthy that the curves for various values of Re all follow the same straight line between their respective Q_{3D} and Q_{2D} with only some deviations at low Q . Furthermore, both Q_{2D} and the plateau value of U_{ls}^2 depend on Re . In figure 6(b), the same data are plotted, but with rescaled axes. The rescaling collapses the data well, with some deviations at small Q related to the convergence of Q_{3D} . This indicates that at large values of Q , U_{ls}^2 scales like $U_{ls}^2 \propto (\epsilon\ell)^{2/3} Re$. This is precisely the scaling of the condensate of 2-D turbulence (Boffetta & Ecke 2012). The critical value where the transition to this maximum value of U_{ls}^2 occurs is $Q_{2D} Re^{-3/4} = \eta/H_{2D} \approx 0.09 - 0.1$.

The scaling allowing us to collapse the data in figure 4 (transient stage) is different from that in figures 6, 8 and 9 (condensate state). This implies that $Q_{2D} \propto Re^{1/2}$ estimated during the early stage of the inverse cascade development is different from $Q_{2D} \propto Re^{3/4}$ estimated at steady state where a condensate is fully developed. The reason for this difference is that the transition to exactly 2-D motion occurs when the maximum shear in the flow (which produces 3-D motion by shear instabilities) is balanced by small-scale viscous dissipation. In the presence of the inverse cascade, an $E(k) \propto \epsilon^{2/3} k^{-5/3}$ spectrum is formed at $k > k_f$, such that the peak of the enstrophy spectrum $k^2 E(k)$ is at the forcing scale. Thus the balance between 2-D shear and 3-D damping is

$$(\epsilon\ell)^{1/3}/\ell \sim \nu/H^2, \quad (3.1)$$

implying $H_{2D} \sim \ell Re^{-1/2}$ (Benavides & Alexakis 2017). In the condensate, however, most of the energy and enstrophy are located in the largest scales and are such that

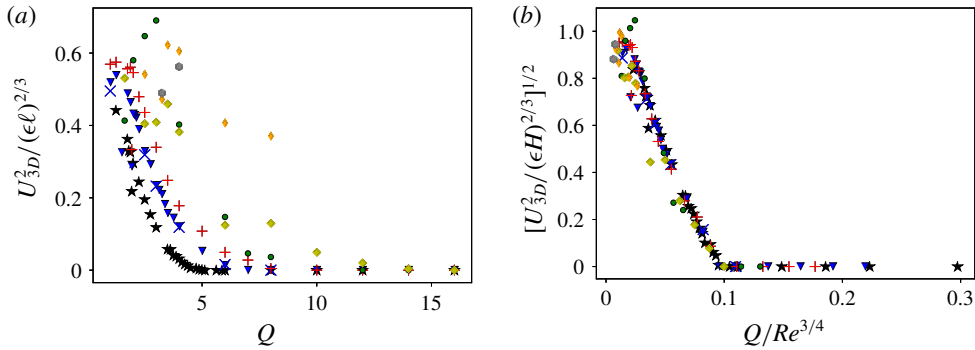


FIGURE 8. (Colour online) (a) U_{3D}^2 as defined in equation (2.7), non-dimensionalised by $(\epsilon \ell)^{2/3}$ and plotted versus Q . (b) The same information as (a), but in terms of the square-root of the 3-D kinetic energy rescaled by $(\epsilon H)^{2/3}$, plotted versus $Q/Re^{3/4}$. This rescaling indicates that $U_{3D}^2 \propto (Q_{2D} - Q)^2$ close to the transition.

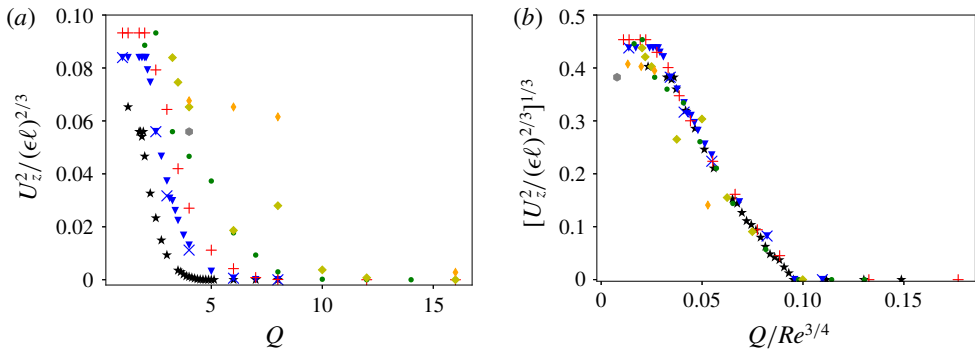


FIGURE 9. (Colour online) (a) U_z^2 as defined in equation (2.6) as a function of Q . (b) The various curves collapse when the abscissa is chosen as $\eta/H = Q/Re^{3/4}$ and the coordinate as $U_{3D}^2 / (\epsilon H)^{2/3}$. Raising the coordinate to the 1/3 power, the curve becomes linear close to onset. This indicates that close to onset, U_z^2 scales as $U_z^2 \approx (Q_c - Q)^3$, where $Q_c \approx 0.09-0.1 \approx Q_{2D}$. We note that the scaling exponent is different from that found for U_{3D}^2 .

energy injection ϵ is balanced by large-scale dissipation $\propto \nu U_{ls}^2 / L^2$. The large-scale shear is thus $U_{ls} / L \propto (\epsilon / \nu)^{1/2}$ which is balanced by the damping rate of 3-D perturbations at onset,

$$(\epsilon / \nu)^{1/2} \sim \nu / H^2, \tag{3.2}$$

giving the scaling $H_{2D} \propto \epsilon^{1/4} \nu^{3/4} \propto \ell Re^{-3/4}$. We will recover the very same steady state scaling in § 6 from a low-order model. These two scalings imply the interesting possibility that a flow which becomes exactly two-dimensional at the early stages of the inverse cascade for $Q \gtrsim Re^{1/2}$ may develop 3-D instabilities at the condensate state if $Q \lesssim Re^{3/4}$.

Figure 8 shows U_{3D}^2 as defined in equation (2.7). In the left panel it is non-dimensionalised by the forcing energy $(\epsilon \ell)^{2/3}$ and plotted versus Q (figure 8a), while in the right panel, it is non-dimensionalised by $(\epsilon H)^{2/3}$, raised to the power 1/2 and

plotted versus $\eta/H = Q/Re^{-3/4}$. Figure 8(a) shows that beyond some non-monotonic behaviour at small Q , U_{3D}^2 decreases monotonically with Q until it reaches zero at Q_{2D} and remains zero beyond this point. The 3-D energy increases with Re at a given Q . Under the rescaling in figure 8(b), the various curves collapse nicely. In particular, the point where U_{3D}^2 vanishes is sharp and identical for all Re , namely $\eta/H \approx 0.1$. Comparing with figure 6(b), one sees that this point and Q_{2D} coincide within the range of uncertainties. This means that beyond Q_{2D} , not only is U_{ls}^2 independent of Q , but also U_{3D}^2 vanishes. This confirms that Q_{2D} corresponds to the point where the motion becomes invariant along z .

Finally, figure 9 shows the vertical kinetic energy, non-dimensionalised by $(\epsilon\ell)^{2/3}$, once plotted versus Q and once taken to the 1/3 power and plotted versus $Q/Re^{3/4}$. The general features of figure 9(a) are similar to figure 8(a): like 3-D energy, vertical kinetic energy decreases with Q until it reaches zero and it increases with Re . The curves collapse in figure 9(b) and the behaviour close to Q_{2D} becomes linear if the coordinate is raised to the 1/3 power, indicating an approximate scaling $U_z^2 \approx (Q_c - Q)^3$ with $Q_c \approx Q_{2D}$. This indicates that the point beyond which the vertical kinetic energy vanishes is close to Q_{2D} , implying that beyond Q_{3D} , the motion is not only invariant along z but also restricted to the x - y plane. Hence, for $Q > Q_{2D}$, the flow has two-dimensionalised exactly.

4. Behaviour close to the transitions: hysteresis and intermittency

In this section, we discuss the behaviour close to the two transition points Q_{2D} and Q_{3D} . Each transition shows a different non-trivial behaviour. Close to Q_{3D} , we observe discontinuous transitions and hysteresis for some range of parameters, while close to Q_{2D} , we find both spatial and temporal intermittency with localised bursts of 3-D energy.

4.1. Close to Q_{3D} : discontinuity and hysteresis

We begin by discussing the behaviour of the flow for Q close to Q_{3D} where a sharp increase of the large-scale energy was observed. This sharp increase could indicate the presence of a discontinuity that could further imply the presence of hysteresis.

To verify the presence of a discontinuity we need perform many different runs varying Q in small steps as well as verifying sensitivity to initial conditions. To do this, a hysteresis experiment has been performed at $Re = 406$, consisting of two series of runs, that we refer to as the ‘upper branch’ and the ‘lower branch’, see figure 10. On the upper branch, we start with random initial conditions and $Q \approx 2.25$ for which the system reaches a condensate equilibrium with an associated non-zero value of large-scale energy. Once the run has equilibrated, we use that equilibrium state to initialise a run at $Q \rightarrow Q - \Delta Q$ with $\Delta Q = 0.1$. By decreasing Q , the physical height of the box is increased. To be able to use the equilibrium state reached at one Q as initial condition for a neighbouring Q , the z -dependence of the velocity field is scaled and the velocity field is projected onto its divergence-free part, formally $v(x, y, z) \rightarrow \mathbb{P}v(x, y, \lambda z)$, where $\mathbb{P} = \mathbb{I} - \nabla^{-2} \nabla(\nabla \cdot)$. Having changed Q and applied this procedure, we let the system equilibrate to a new condensate state. This is repeated five more times (step size reduced to $\Delta Q = 0.05$ and then $\Delta Q = 0.025$) down to $Q \approx 1.9$. When Q is now lowered 0.025 further, the condensate decays into 3-D turbulence and the large-scale energy saturates to close to zero. Reducing Q even more, U_{ls}^2 remains small, indicating a 3-D turbulent state. The lower branch was calculated similarly, with the only difference that the experiment started at low Q and Q was increased

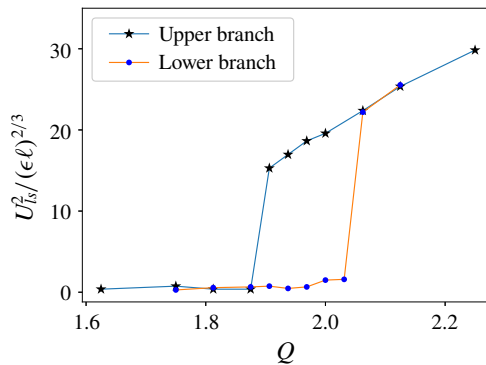


FIGURE 10. (Colour online) Hysteresis curve of U_{ls}^2 non-dimensionalised by the forcing energy. Two experiments are shown, the ‘lower branch’ starting from small Q (deep layer) and increasing Q and the ‘upper branch’ starting from large Q (thin layer) and decreasing Q .

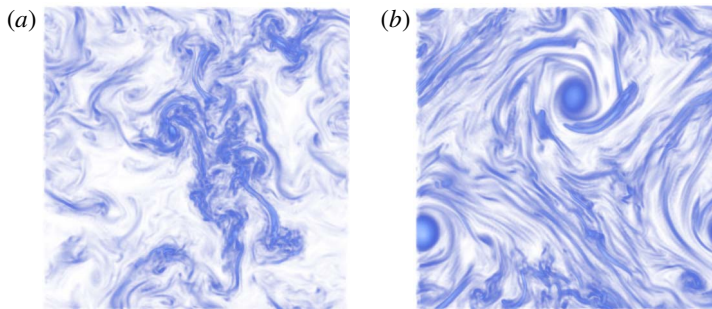


FIGURE 11. (Colour online) Visualisation of the typical flow field after long simulation time at $Q \approx 1.97$ in the hysteresis experiment on the upper (b) and lower (a) branches. The lower branch flow field shows small-scale structures and no large-scale organisation, reminiscent of 3-D turbulence. By contrast, the upper branch flow field is characterised by two large-scale vortices in addition to smaller-scale structures in between them.

in steps of 0.05 and then of 0.025. For small Q , the two branches coincide, while the lower branch remains at low U_{ls}^2 (3-D turbulence) up to $Q \approx 2.025$. For Q larger than $Q = 2.025$, the lower branch merges with the upper branch, closing the hysteresis loop and a condensate is spontaneously formed from 3-D turbulence. In other words, for $Re = 406$ in the range $1.9 \leq Q \leq 2.025$, there are multiple steady states and to which state the system will saturate depends on the initial conditions. The flow field for two such states starting from different initial conditions for $Q \approx 1.97$ is visualized in figure 11.

The following remarks are in order: although for each Q we ran the simulations until saturation was achieved, since we are dealing with a noisy system, rare transitions can exist between the two branches of the hysteresis loop. To test this, we picked the point $Q \approx 1.97$ on both lower and upper branches and ran them for a long time (thousands of eddy turnover times $\tau = (L^3/\epsilon)^{1/2}$). In neither case did we see a transition between the two branches, indicating that such transitions are rare (if not

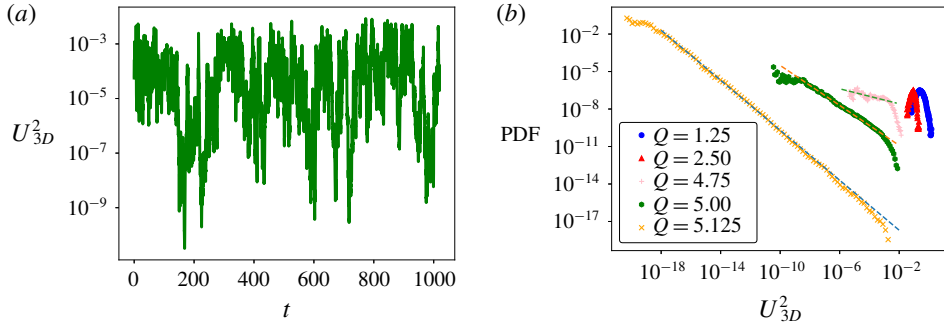


FIGURE 12. (Colour online) Plots showing temporal intermittency at $Re = 203$. (a) Shows a typical time series (on linear–log axes) of 3-D energy close to Q_{2D} . Specifically, $Q = 5$, while $Q_{2D} \approx 5.13$ at this value of Re . (b) Shows probability density functions (PDFs) corresponding to this time series as well as for different values of Q (PDFs shifted by a constant factor for better visibility). The different symbols mark different values of Q , while the dotted lines correspond to power laws with exponents -1 (bottom), -0.8 (middle) and -0.3 (top) respectively.

absent) in the middle of the hysteresis loop. Near the edges of the hysteresis loop at $Q \approx 2.05$ and $Q \approx 1.9$, the dependence on simulation time is likely to be stronger, but this has not been investigated.

Furthermore, we note that the bifurcation diagram of figure 10 corresponds to a relatively low Reynolds number $Re = 406$. Whether this subcritical behaviour persists at larger Re and/or larger box sizes (smaller K) is still an open question. Figure 7 suggests that a discontinuity continues to exist at $Q = Q_{3D}$ up to high Reynolds numbers ($Re = 2031$ shown there). In addition, we found more points at higher Re that showed a dependence on initial conditions but without having enough values of Q to create a hysteresis diagram. These findings suggest that subcritical behaviour and hysteresis might survive even at high Re . However, due to the high computational cost at higher resolution and the long duration of the runs required to verify that the system stays in a particular state, we could not investigate this possibility in detail. Further simulations at larger Re and possibly smaller K (larger boxes) are required to resolve this issue. Similar hysteretic behaviour has recently been reported in rotating turbulence, see Yokoyama & Takaoka (2017). More generally, multistability is observed in many turbulent flows, see Weeks *et al.* (1997), Ravelet *et al.* (2004) as examples.

4.2. Close to Q_{2D} : intermittent bursts

Next, we discuss the behaviour of the flow close to the second critical point Q_{2D} . A typical time series of 3-D energy for $Q \lesssim Q_{2D}$ is shown in figure 12(a). One observes bursty behaviour and variations over many orders of magnitude, indicating on–off intermittency (Fujisaka & Yamada 1985; Platt, Spiegel & Tresser 1993). On–off intermittency refers to the situation where a marginally stable attractor loses or gains stability due to noise fluctuations. When instability is present, a temporary burst is produced before the system returns to the attractor. On–off intermittency predicts that the unstable mode X follows a power-law distribution $P(X) \propto X^{\delta-1}$ for $X \ll 1$ where δ measures the deviation from onset (here $\delta \propto (Q_{2D} - Q)/Q_{2D}$) and all moments scale linearly with the deviation $\langle X^n \rangle \propto \delta$.

In our system, the 2-D flow forms the marginal stable attractor that loses stability to 3-D perturbations depending on the exact realisation of the 2-D turbulent flow. To formulate this, we decompose the velocity field into its 2-D and 3-D parts, $\mathbf{u} = \mathbf{u}_{2D} + \mathbf{u}_{3D}$, where the 2-D part is defined as the Fourier sum of \mathbf{u} restricted to modes with $k_z = 0$. Filtering the 3-D component of equation (2.1b), dotting with \mathbf{u}_{3D} and integrating over the domain gives

$$\frac{1}{2} \partial_t U_{3D}^2 = -\langle \{\mathbf{u}_{3D} \cdot \nabla \mathbf{u}_{2D}\} \cdot \mathbf{u}_{3D} \rangle - \nu \langle |\nabla \mathbf{u}_{3D}|^2 \rangle, \tag{4.1}$$

where $\langle \cdot \rangle$ denotes integration over the domain. The chaotic 2-D motions then act as multiplicative noise while the viscous terms provide a mean decay rate. An important physical mechanism for creating 3-D disturbances is 3-D elliptic instability of the 2-D counter-rotating vortex pair forming the condensate, as described in Le Déz & Laporte (2002). This may explain the presence of the critical value Q_{2D} itself: instability requires small vertical wavenumbers, but the minimum wavenumber increases with decreasing H and Q_{2D} corresponds to the point where 3-D perturbations begin to decay.

Figure 12 shows that temporal intermittency is present in the thin-layer system. Panel (a) shows a typical time series of 3-D energy at $Q \lesssim Q_{2D}$ which fluctuates over six orders of magnitude. In particular, as mentioned before, there are burst-like excursions in 3-D energy. In figure 12(b), PDFs constructed from this time series and similar ones for different values of Q are shown along with dotted lines indicating power laws with exponents -1 , -0.8 and -0.3 . The PDFs are very close to a power law for a significant range of U_{3D}^2 and the exponent converges to minus one as the transition is approached, in agreement with on-off intermittency predictions. However, the scaling of 3-D energy with deviation from onset shown in figure 8(b) does not follow the linear prediction of on-off intermittency, but rather $\langle U_{3D}^2 \rangle \propto (Q_{2D} - Q)^2$. For U_z^2 , figure 9 seems to suggest yet a different scaling, namely $\langle U_z^2 \rangle \propto (Q_{2D} - Q)^3$. A similar behaviour was also found in Benavides & Alexakis (2017) and was attributed to the spatio-temporal character of the intermittency that not only leads to 3-D motions appearing more rarely in time as criticality is approached but also to them occupying a smaller fraction of the available volume. This appears also to be the case in our results, as demonstrated in figures 13 and 14, where \mathbf{u}_{3D}^2 and the vertical velocity u_z are plotted for three different values of Q . As Q approaches the critical value Q_{2D} , the structures become smaller for \mathbf{u}_{3D}^2 and u_z with the difference that \mathbf{u}_{3D}^2 shows spot-like structures in figure 13(c) which are absent for u_z . This difference may be related to the two different scalings observed for U_{3D}^2 and U_z^2 with $Q_c - Q$ small: if the volume fraction of vertical motion depends on $Q_c - Q$ to a different power than that of vertical variations, two different behaviours of U_z^2 and U_{3D}^2 would follow. A more detailed quantitative investigation of the scaling of volume fraction will be needed to clarify this.

In summary, we have found non-trivial behaviour close to both transitions: we have observed hysteresis near Q_{3D} and spatio-temporal intermittency close to Q_{2D} where the temporal behaviour seems to be described by on-off intermittency. Taking into account these effects will be crucial for understanding the exact nature of the observed transitions.

5. Spectra and fluxes

In this section, we discuss the spectral space properties of the three different regimes described in the previous section. For this purpose, it is necessary to define

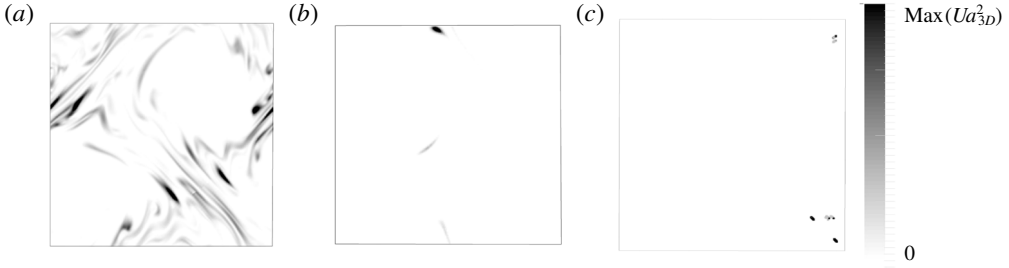


FIGURE 13. Snapshots of u_{3D}^2 for $Re = 203$ and $Q = 2.5$ (a), $Q = 5.0$ (b) and $Q = 5.125$ (c) (corresponding to figure 12). The colour bar is chosen in each plot such that the maximum value of u_{3D}^2 is shown in black. As Q increases towards $Q_{2D} \approx 5.13$, U_{3D}^2 becomes more and more localised. In (c), u_{3D}^2 is concentrated in small columnar structures (upper and lower right-hand corner) absent in figure 14(c).

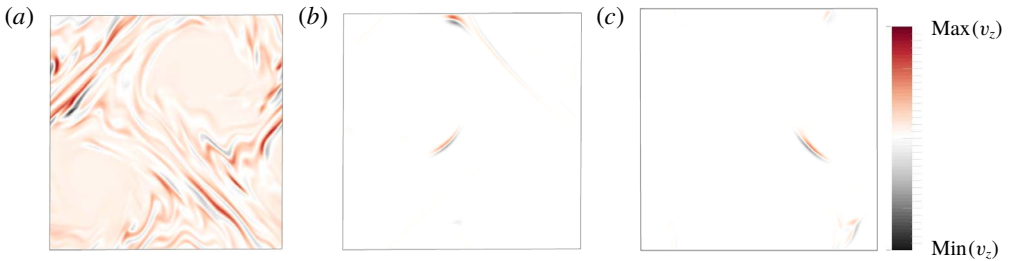


FIGURE 14. (Colour online) Snapshots of v_z for $Re = 203$ and $Q = 2.0$ (a), $Q = 5.0$ (b) and $Q = 5.125$ (c). The colour scale on the right is chosen in each plot such that the minimum (negative) is shown in black and the maximum (positive) in red. (same as in figure 12). As in figure 13, u_z becomes localised in smaller and smaller areas as Q increases, i.e. there is increasing spatial intermittency as $Q_{2D} \approx 5.13$ is approached.

a few additional quantities. In addition to the total 1-D energy spectrum defined in (2.3), is of interest to consider the two-dimensional energy spectrum in the (k_h, k_z) plane.

$$E(k_h, k_z) = \frac{1}{2} \sum_{\substack{k' \\ k_x'^2 + k_y'^2 = k_h^2 \\ k_z' = k_z}} |\hat{u}_{k'}|^2. \tag{5.1}$$

Moreover, the total 1-D energy spectrum may advantageously be split up into three components: the energy spectrum of the (vertically averaged) 2D2C field

$$E_h(k_h) = \frac{1}{2} \sum_{\substack{k \\ k_x^2 + k_y^2 = k_h^2 \\ k_z = 0}} (|\hat{u}_k^{(x)}|^2 + |\hat{u}_k^{(y)}|^2), \tag{5.2}$$

the energy spectrum of the (vertically averaged) vertical velocity

$$E_z(k_h) = \frac{1}{2} \sum_{\substack{k \\ k_x^2 + k_y^2 = k_h^2 \\ k_z = 0}} |\hat{u}_k^{(z)}|^2, \tag{5.3}$$

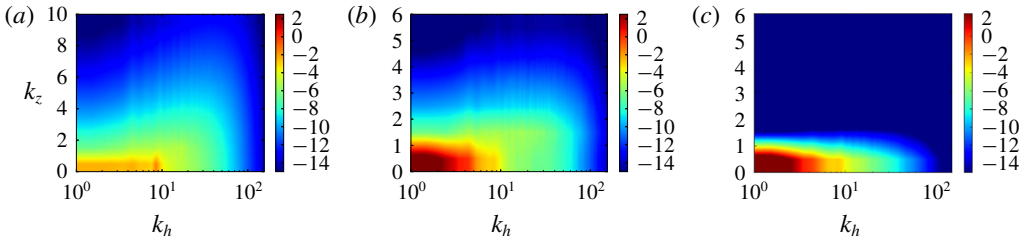


FIGURE 15. (Colour online) Logarithmic surface plots of $E(k_h, k_z)$ at steady state in the three regimes (a) $Q < Q_{3D}$, (b) $Q_{3D} < Q < Q_{2D}$ and (c) $Q_{2D} < Q$.

and the energy spectrum of the 3-D flow defined as

$$E_{3D}(k_h) = \frac{1}{2} \sum_{\substack{k \\ k_x^2 + k_y^2 = k_h^2 \\ k_z \neq 0}} |\hat{\mathbf{u}}_k|^2, \tag{5.4}$$

satisfying $E_{tot}(k_h) = E_h(k_h) + E_z(k_h) + E_{3D}(k_h)$. Furthermore, we introduce three different quantities related to spectral energy flux. First, the total energy flux as a function of horizontal wavenumber

$$\Pi(k_h) = \langle \mathbf{u}_{k_h}^< \cdot (\mathbf{u} \cdot \nabla) \mathbf{u} \rangle, \tag{5.5}$$

where the low-pass filtered velocity field is

$$\mathbf{u}_{k_h}^< = \sum_{\substack{k \\ k_x^2 + k_y^2 < k_h^2}} \hat{\mathbf{u}}_k e^{ik \cdot \mathbf{x}}. \tag{5.6}$$

With this definition, $\Pi(k_h)$ expresses the flux of energy through the cylinder $k_x^2 + k_y^2 = k_h^2$ due to the nonlinear interactions. The 2-D energy flux as a function of k_h is defined as

$$\Pi_{2D}(k_h) = \langle \bar{\mathbf{u}}_{k_h}^< \cdot (\bar{\mathbf{u}} \cdot \nabla) \bar{\mathbf{u}} \rangle, \tag{5.7}$$

where the over-bar stands for vertical average and expresses the flux through the same cylinder due to only 2D2C interactions. Finally, we define the 3-D energy flux (due to all interactions other than those in (5.7)) as a function of horizontal wavenumber by

$$\Pi_{3D}(k_h) = \Pi(k_h) - \Pi_{2D}(k_h). \tag{5.8}$$

It expresses the flux due to all interactions other than the ones in (5.7).

Figure 15 shows the steady state 2-D energy spectrum in the three different regimes: (a) $Q < Q_{3D}$, (b) $Q_{3D} < Q < Q_{2D}$ and (c) $Q_{2D} < Q$. In the 3-D turbulent case (a), the global maximum is at the forcing scale and $k_z = 0$, while large k_z modes have a relatively larger fraction of total energy than in cases (b,c). In cases (b,c), a condensate is present with a maximum at the largest wavenumber $k_h = 1$, $k_z = 0$. In case (b), there is still energy in the $k_z \neq 0$ modes, while in case (c), the energy is entirely concentrated in the $k_z = 0$ mode. Figure 16 shows the energy spectra $E_h(k_h)$, $E_z(k_h)$ and $E_{3D}(k_h)$ for the same three cases (a–c). In case (a) (3-D turbulence), all three spectra are of the same order, with a small excess of $E_h(k_h)$ in the large scales and an

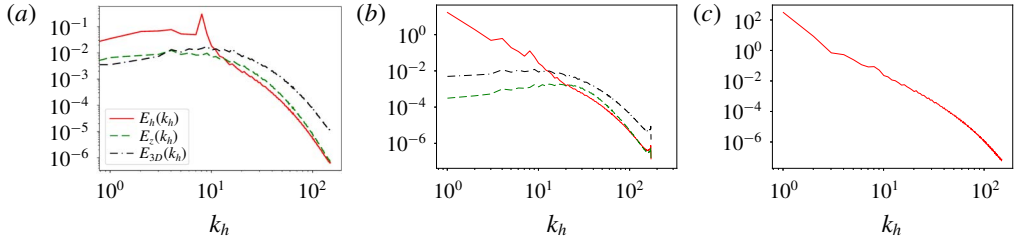


FIGURE 16. (Colour online) Three different energy spectra, $E_h(k_h)$, $E_z(k_h)$, $E_{3D}(k_h)$ at $Re = 609$ for 3-D turbulence (a), 2-D turbulence (c) and an intermediate case $Q \in (Q_{3D}, Q_{2D})$ (b) flux-loop condensate (cf. main text). For 3-D turbulence ($Q = 1.25 < Q_{3D}$), the 2-D energy spectrum peaks at the forcing scale and is an order of magnitude bigger than the other components. In the flux-loop condensate ($Q = 4$), 2-D energy is maximum at $k = 1$ and 3-D energy and vertical energy are non-zero. In 2-D turbulence ($Q = 16 > Q_{2D}$), 2-D energy is maximum at $k = 1$, but 3-D energy and vertical energy vanish.

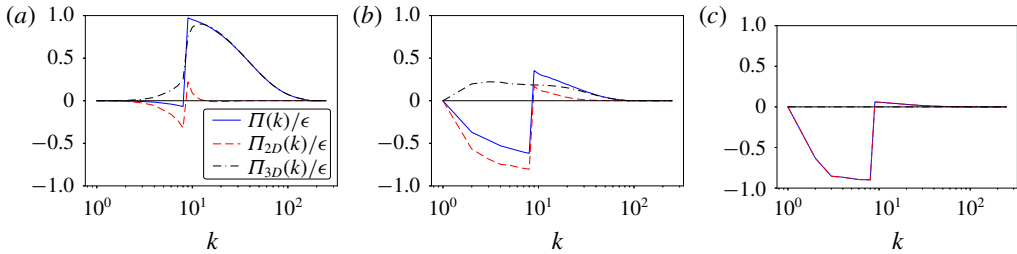


FIGURE 17. (Colour online) Three different components of spectral energy flux, $\Pi(k_h)$, $\Pi_{2D}(k_h)$ and $\Pi_{3D}(k_h)$, are shown for the same three cases and in the same order as in figure 16.

excess of $E_{3D}(k_h)$ in the small scales. The small scale separation between the forcing and the dissipation scale does not allow us to observe a $k^{-5/3}$ power-law regime. In case (b), $E_h(k_h)$ clearly dominates in the large scales, forming a steep spectrum (close to $E_h(k_h) \propto k_h^{-4}$). However, at wavenumbers larger than the forcing wavenumber $k_f = 8$, $E_z(k_h)$ and $E_{3D}(k_h)$ become of the same order as $E_h(k_h)$. In case (c) (2-D turbulence), where $Q > Q_{2D}$, the spectra $E_z(k_h)$ and $E_{3D}(k_h)$ have reduced to values close to the round-off error and are not plotted. The 2-D spectrum $E_h(k_h)$ displays again a steep power-law behaviour close to $E_h(k_h) \propto k_h^{-4}$.

Figure 17 shows the energy fluxes as defined in equations (5.5)–(5.8) for the same three cases examined in figure 16. In panel (a), where the case $Q < Q_{3D}$ is examined, there is almost no inverse flux of energy and $\Pi(k_h < k_f)$ is practically zero. The small inverse flux that is observed for $\Pi_{2D}(k_h)$ at $k < k_f$ does not reach the largest scale of the system and is nearly completely balanced by $\Pi_{3D}(k_h)$, which is forward. At wavenumbers larger than k_f , the total flux is positive and is completely dominated by Π_{3D} . This is to be contrasted with the rightmost panel (c) with $Q > Q_{2D}$, where at small wavenumbers, the flux is negative and is dominated by the 2-D flow, while at large wavenumbers there is a very small forward flux. For the intermediate case $Q_{3D} < Q < Q_{2D}$ in panel (b), there is an inverse energy flux. This flux can be decomposed into a negative 2-D part $\Pi_{2D}(k_h)$ and a positive 3-D part $\Pi_{3D}(k_h)$. In other words, the

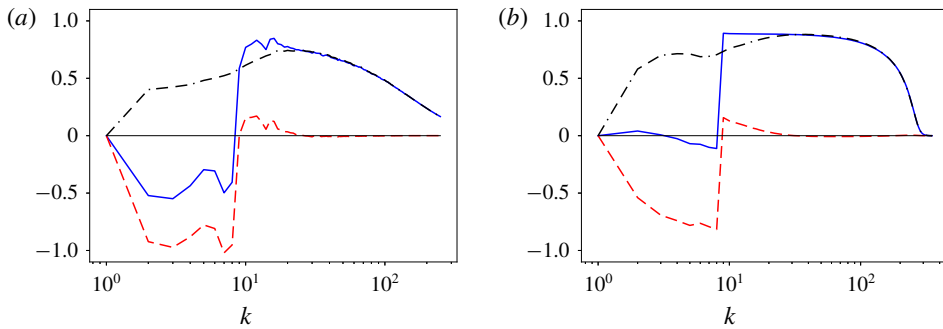


FIGURE 18. (Colour online) Flux-loop condensate steady state fluxes for $Re = 4062$ in (a) and the hyper-viscous run in (b).

2-D components of the flow bring energy to the largest scales of the system, which is then brought back to the small scales by the 3-D components of the flow associated with a forward energy flux, thus forming a loop for the energy transfer. For this reason, we refer to this case as flux-loop condensate.

Due to finite viscosity, part of the energy that arrives at the largest scale (shown in figure 17*b*) is dissipated. Therefore, the two fluxes are not completely in balance. As Re is increased, however, the fraction of the energy that is dissipated in the large scales is decreased and the two opposite fluxes come closer to balancing each other. This is shown in figure 18, where the energy fluxes for the highest Re simulation and for the simulation with hyper viscosity are plotted. The two opposite directed fluxes are closer in amplitude. At $Re \rightarrow \infty$ it is thus expected that the inverse and forward fluxes at large scales will be in perfect balance and all the energy is dissipated in the small scales. It is worth noting, however, that the inverse cascade (negative flux) due to the 2-D components has much stronger fluctuations than the forward cascading flux that has led to the non-monotonic behaviour of the flux observed in figure 18 at small k due to insufficient time averaging.

6. A three-mode model

In this section, we formulate and analyse a simple three-scale ordinary differential equation (ODE) model which reproduces certain features of the DNS results described in § 3.

As illustrated in figure 19, our model comprises a 2-D mode U_{2D} at the scale L of the domain, a mode U_f at the forcing scale ℓ and a 3-D mode U_{3D} at the scale of the layer height H , whose interactions are spectrally non-local, thus taking into account a major result from § 5. The model describes the system at steady state where these scales are well separated, but is not expected to capture the transient phase where all intermediate scales between L and ℓ participate due to the inverse cascade. As before, let $Q = \ell/H$, $K = \ell/L$ and $Re = (\epsilon \ell^4)^{1/3}/\nu$. Interactions between modes are modelled using eddy viscosity, which amounts to modifying the molecular viscosity ν by terms involving the small-scale velocities, modelling the effect of small-scale motions on large-scale motions as diffusive. The conceptual foundations of eddy viscosity were laid by de Saint Venant in his effective viscosity, (de Saint-Venant 1843) (see Darrigol (2017) for a historical review). Eddy viscosity was quantified for the first time by Boussinesq (1877) and later widely popularised through the works of Taylor (Taylor 1915, 1922), see also Kraichnan (1976). It has been estimated in

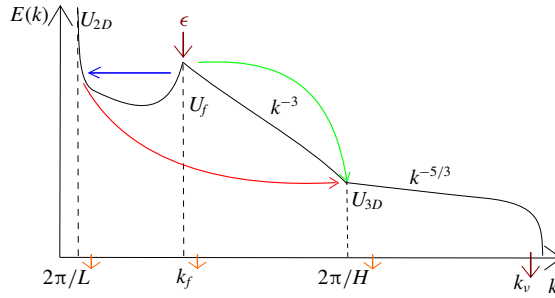


FIGURE 19. (Colour online) Sketch of three-mode model. Solid curve: energy spectrum $E(k)$ of the condensate state. The energy injected at k_f at a rate ϵ is distributed between large and small scales. Moreover, energy is transferred from large to small scales. Finally viscous dissipation occurs at all scales since $Re < \infty$ (short arrows on abscissa) and energy is transferred to the dissipation range (arrow at $k_v = 2\pi/\eta$). The spectrum $E(k)$ shares certain features with figure 1(e) of Xia *et al.* (2011) and figure 3 of Celani *et al.* (2010).

various limits both in 2-D and 3-D flows (Meshalkin 1962; Sivashinsky & Yakhot 1985; Bayly & Yakhot 1986; Yakhot & Sivashinsky 1987; Hefer & Yakhot 1989; Dubrulle & Frisch 1991; Gama, Vergassola & Frisch 1994; Cameron, Alexakis & Brachet 2016; Alexakis 2018).

There are two notable cases where the dependence of eddy viscosity ν_E on the flow amplitude U_s and length scale l_s is known. For $Re \rightarrow \infty$, one expects that ν_E becomes independent of ν and the only dimensionally consistent possibility for ν_E is given by

$$\nu_E = c_1 U_s l_s, \tag{6.1}$$

where c_1 is a non-dimensional number. In the low- Re limit, on the other hand, an exact asymptotic expansion can be carried out (see Dubrulle & Frisch 1991) which reveals that

$$\nu_E = c_2 \frac{U_s^2 l_s^2}{\nu} + O(U_s^4 l_s^4 / \nu^2), \tag{6.2}$$

where the non-dimensional number c_2 can be evaluated by the expansion. It may seem counter-intuitive that the low- Re limit could have any relevance for the turbulent problem, but since we have established in the DNS that the presence of Q_{2D} is a finite- Re phenomenon ($Q_{2D} \propto Re^{3/4}$), we clearly need to include a finite Re ingredient to describe it and the exact result (6.2) is selected for this purpose. The sign of the prefactors c_1, c_2 depends on the exact form of the small-scale flow and in particular its dimensionality. While 2-D flows tend to have negative eddy viscosities and transfer energy upscale, 3-D flows are expected to have positive eddy viscosities and transfer energy downscale. For our model, we are going to consider that interactions among the three different scales $L > \ell > H$ are such that the flow at the smaller scale acts as an eddy viscosity on the flow at the larger scale. These interactions are illustrated in figure 19. In particular, the energy injected at the forcing scale k_f at a rate ϵ is transferred both to the large scale L (by a negative eddy viscosity $-\mu$) and to the small scales (by a positive eddy viscosity σ). The large scales lose energy directly to the small scales (via a positive eddy viscosity term η), while the small scales dissipate energy by transfer to the dissipation range, modelled by a nonlinear energy sink.

In addition, viscosity is finite, such that all scales dissipate locally. The set of equations below formalises these ideas:

$$\frac{d}{dt}U_{2D}^2 = -(v - \mu + \eta)\frac{U_{2D}^2}{L^2}, \tag{6.3a}$$

$$\frac{d}{dt}U_f^2 = \epsilon - (v + \sigma)\frac{U_f^2}{\ell^2} - \mu\frac{U_{2D}^2}{L^2}, \tag{6.3b}$$

$$\frac{d}{dt}U_{3D}^2 = \eta\frac{U_{2D}^2}{L^2} + \sigma\frac{U_f^2}{\ell^2} - \frac{U_{3D}^3}{H} - v\frac{U_{3D}^2}{H^2}. \tag{6.3c}$$

Note in particular that eddy viscosities do not dissipate energy, but merely redistributes it between different scales. Adding the three model equations leads to

$$\frac{d}{dt}(U_{2D}^2 + U_f^2 + U_{3D}^2) = \epsilon - v\left(\frac{U_{2D}^2}{L^2} + \frac{U_f^2}{\ell^2} + \frac{U_{3D}^2}{H^2}\right) - \frac{U_{3D}^3}{H}, \tag{6.4}$$

showing that the total kinetic energy only changes due to molecular viscosity v , energy injection ϵ and the sink term representing the 3-D energy cascade to the dissipation range, U_{3D}^3/H . Depending on Re , either of the two expressions for eddy viscosity (6.1), (6.2) may be expected to yield an adequate description of the multi-scale interactions in the problem. A model that interpolates smoothly between the large and small v limits, thus taking into account the finite- Re information necessary for describing Q_{2D} , is given by

$$\mu = \alpha\frac{U_f^2\ell^2}{v + U_f\ell}, \quad \eta = \beta\frac{U_{3D}^2H^2}{v + U_{3D}H}, \quad \sigma = \gamma\frac{U_{3D}^2H^2}{v + U_{3D}H}, \tag{6.5a-c}$$

with $\alpha, \beta, \gamma > 0$ non-dimensional coupling constants. In the limits $v \rightarrow 0$ and $v \rightarrow \infty$, the above expressions converge to the formulae for eddy viscosities described before. The nonlinear dynamical system thus defined possesses a varying number of fixed points depending on parameters. To classify them, first note that $\epsilon \neq 0 \Rightarrow U_f \neq 0$ at any fixed point by (6.3b) and the definition of μ in (6.5). Hence there are four possibilities:

- (i) laminar state: $U_{2D} = U_{3D} = 0$ (all energy in forcing scale),
- (ii) three-dimensional turbulence state: $U_{2D} = 0$ and $U_{3D} \neq 0$,
- (iii) two-dimensional condensate state: $U_{2D} \neq 0$ and $U_{3D} = 0$ and
- (iv) flux-loop condensate state: $U_{2D} \neq 0$ and $U_{3D} \neq 0$.

As shown in § A.1, in the zero viscosity limit, there is neither a laminar state nor a 2-D condensate fixed point in the model. This emphasises the importance of including finite- Re information into the model for describing both Q_{3D} and Q_{2D} in a single model. The laminar state appears for values of $Re \equiv (\epsilon\ell^4)^{1/3}/v$ below a critical value Re_c for which there is no transfer, neither to large nor to small scales. Above this critical value, one of the three other states is stable, depending on the value of $Q = \ell/H$. For small values of Q (large H), the system is in the 3-D turbulence state, where energy is only exchanged between the forcing scale ℓ and the small scale H . Above the critical value Q_{3D} , the system transitions to the flux-loop condensate state where part of the injected energy is transferred to the large scales and then back to the small scales, thus forming a loop. Finally, at sufficiently large Q above a second critical point Q_{2D} , the system transitions to the 2-D condensate where it follows 2-D dynamics and there is only a transfer of the injected energy to the large scales.

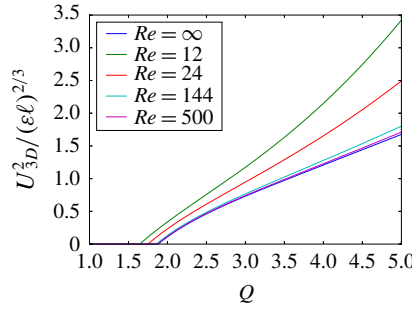


FIGURE 20. (Colour online) Steady state U_{3D}^2 from the full model for four different Re as well as for the $Re = \infty$ limit. The $Re = 500$ and the $Re = \infty$ cases are almost indistinguishable. The parameters used are $L = \ell = 1$, $\alpha = 1$, $\beta = 5$, $\gamma = 0.5$.

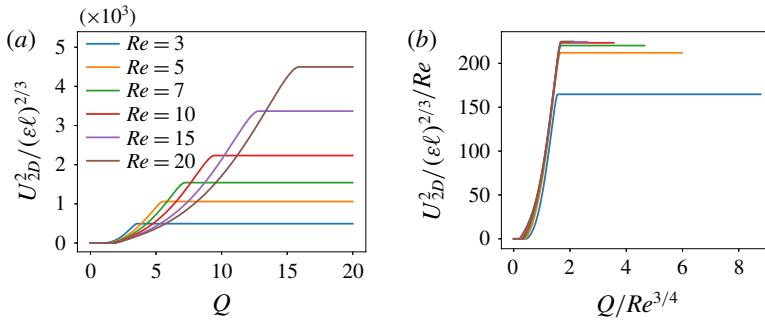


FIGURE 21. (Colour online) Model steady state U_{2D}^2 with and without rescaling. The overall structure of the plots is strongly reminiscent of corresponding DNS results in figure 6(a,b). In (a), U_{2D} vanishes at small Q , increases monotonically between Q_{3D} and Q_{2D} and remains constant for $Q > Q_{2D}$. (b) Shows the same data as (a) with the abscissa rescaled by $Re^{3/4}$ and the coordinate rescaled by Re as in figure 6(b). The collapse improves with increasing Re . Parameters: $\alpha = 0.51$, $\beta = 8$, $\gamma = 0.1$, $\ell = L/15 = 1$.

From this simple model, three major predictions may be derived:

- (i) Firstly, the critical point Q_{3D} is predicted to converge to a Re -independent value at large Re as is shown in figure 20. In fact, in the infinite Re limit of the model, there remains only one bifurcation, namely that at Q_{3D} between two-dimensional turbulence and the split cascade state.
- (ii) Secondly, the critical point Q_{2D} is predicted to obey

$$Q_{2D} \propto Re^{3/4}. \tag{6.6}$$

- (iii) Thirdly, for $Q > Q_{2D}$, i.e. in the 2-D turbulent state, the steady state energy is predicted to be

$$U_{2D}^2 = (\epsilon \ell)^{2/3} \left(\frac{L}{\ell}\right)^2 Re. \tag{6.7}$$

The detailed derivations of these results are given in § A.1. All these three main features are in agreement with the DNS and therefore the diagram that displays the different phases of the model, shown in figure 21(a), resembles the corresponding

figure 6(a) from the DNS. Indeed, the same rescaling collapses the curves in both cases, see figures 6(b) and 21(b). We also note that for $0 < Q_{2D} - Q \ll 1$, it is predicted that $U_{3D}^2 \sim (Q_{2D} - Q)^2$ (see § A.2), again in agreement with the DNS.

We understand the present ODE model as a mean-field description which captures the global system behaviour and averaged quantities, but does not take fluctuations into account. Due to the importance of fluctuations near criticality, the ODE model does not reproduce the detailed behaviour there. However, when a fluctuating energy input is taken into account by replacing $\epsilon \rightarrow \epsilon + \sigma \zeta$ in (6.3b) (ζ being white Gaussian noise), on-off intermittency is found close to Q_{2D} where the PDF of U_{3D}^2 follows a power law with an exponent tending to -1 as $Q \rightarrow Q_{2D}$ from below (see § A.3), just as in the DNS. This is a consequence of the structure of the model equations.

To conclude this section, we reiterate that the model presented above successfully captures the location of the critical points (up to a scaling factor) as well as the amplitude of the condensate U_{2D}^2 , while not producing a hysteresis. The intermittency close to Q_{2D} found in DNS is reproduced by the model when additive noise is included.

7. Conclusions

We present the first detailed numerical study of the steady state of thin-layer turbulence as a function of the system parameters using an extensive set of high-resolution simulations.

It is shown that the split cascade observed at early times of the flow evolution (Celani *et al.* 2010; Benavides & Alexakis 2017; Musacchio & Boffetta 2017) leads to the formation of condensate states in the long-time limit. Three different states were found for large Re . (i) For very thick layers the system saturates in a regular 3-D turbulence state with no inverse cascade and negligible dissipation at large scales. (ii) At intermediate-layer thickness, a flux-loop condensate is formed in which part of the energy transferred to the condensate by the 2-D motions is transferred back to the small scales by the 3-D motions. (iii) For very thin layers, the system becomes two-dimensional and forms a 2-D-turbulence condensate, where the inversely cascading energy is balanced by the dissipation due to viscosity at large scales. The transition from 3-D turbulence to the flux-loop condensate occurs at a critical height H_{3D} (Q_{3D}) that is a decreasing (increasing) function of Re , but saturates at a Re independent value for large Re . For values of H slightly smaller than H_{2D} the amplitude of the large-scale velocity U_{ls}^2 jumps discontinuously to a large value and increases linearly after that. Close to the threshold, a hysteresis diagram was constructed where the system saturates to a different attractor (3-D turbulence or flux-loop condensate) depending on the initial conditions. Whether this hysteresis behaviour persists at larger Re and larger box sizes $1/K$ remains an open question. The flux-loop condensate transitions to a 2-D turbulence condensate at a critical height H_{2D} that scales like $H_{2D} \propto \ell Re^{-3/4}$ unlike the early stages of the development where $H_{2D} \propto \ell Re^{-1/2}$ (Benavides & Alexakis 2017). For the 2-D turbulence condensate, the large-scale energy was found to be inversely proportional to Re and independent from H . The transition from a flux-loop condensate to a 2-D turbulence condensate showed strong spatio-temporal intermittency leading to a scaling of the average 3-D energy as the square of the deviation from onset $U_{3D}^2 \propto (H - H_{2D})^2$, similarly as in Benavides & Alexakis (2017).

A three-mode model has been proposed which reproduces the DNS scalings of the critical points H_{2D} and H_{3D} as well as the amplitude of the condensate in the 2-D

turbulence regime. The model demonstrates the basic mechanisms involved: a 2-D flow that moves energy from the forcing scale to the condensate and a 3-D flow that takes away energy both from the large scales and the forcing scales. The model does not describe bi-stability or discontinuity close to Q_{3D} . Nonetheless, it captures the occurrence of both transitions observed in the DNS and provides several correct quantitative predictions.

We stress once more that the present work is the first numerical study of thin-layer turbulent condensation. Previous studies of the thin-layer problem were restricted to the transient inverse cascade regime due to the long computation time needed to reach the condensate state. Therefore, the present study is novel and provides an important first step towards a better understanding of thin-layer turbulent condensates (of which the Earth's atmosphere and ocean may be viewed as examples, despite the idealised nature of our set-up), many open questions remain. The complexity of the physics involved close to criticality goes beyond the mean-field model and requires further targeted studies. We are convinced that both critical points deserve more detailed investigations by means of numerical simulations, experiments and modelling. Another important remaining open problem is the formation of an inverse cascade from a 3-D forcing. To study this, the amplitude of the 3-D components of the forcing should be varied compared to the 2-D components in a future study. Three-dimensional forcing will make a connection with more natural forcing mechanisms like convection that also display condensates (Favier *et al.* 2014; Guervilly *et al.* 2014; Rubio *et al.* 2014).

Concerning the realisability of the present numerical results in an experiment, it needs to be stressed that this study only considers the triply periodic domain for simplicity. When attempting to transfer the results to no-slip boundary conditions, a word of caution is therefore in order: viscous boundary layers may lead to large-scale drag, which is explicitly left out from the model set-up used here. Also, 3-D turbulence in boundary layers may infect the interior flow, thereby affecting even high wavenumbers and the two-dimensionalisation even in the bulk of the flow. However, the wealth of experimental observations of turbulent condensates in thin layers, as referenced in the introduction and summarised in Xia & Francois (2017), suggests that the condensation phenomenon at finite height is robust between different boundary conditions as well as between the different forcing methods used in experiment and numerical simulations. In particular, it would be very interesting to probe the discontinuity and associated phenomena reported here in an experiment. This has not been done before and experimental studies of thin-layer turbulent condensates have the advantage of allowing higher Reynolds numbers and much better time statistics.

Acknowledgements

We thank three referees for their helpful and valuable suggestions which have helped to improve this paper substantially. This work was granted access to the HPC resources of MesoPSL financed by the Région Ile de France and the project Equip@Meso (reference ANR-10-EQPX-29-01) of the programme Investissements d'Avenir supervised by the Agence Nationale pour la Recherche and the HPC resources of GENCI-TGCC-CURIE & CINES Occigen (Project no. A0010506421, A0030506421 and A0050506421) where the present numerical simulations have been performed. This work has also been supported by the Agence nationale de la recherche (ANR DYSTURB project no. ANR-17-CE30-0004). A.v.K. was supported by Deutscher Akademischer Austauschdienst and Studienstiftung des deutschen Volkes.

Appendix A. Derivation of mean-field model predictions

A.1. Scalings of critical points and condensate amplitude

In the low viscosity limit, the eddy viscosities given in equation (6.5), take the form (6.1) and the resulting system of equations reads

$$\partial_t U_{2D}^2 = \frac{(\alpha U_f \ell) U_{2D}^2}{L^2} - \frac{(\beta U_{3D} H) U_{2D}^2}{L^2}, \tag{A 1a}$$

$$\partial_t U_f^2 = \epsilon - \frac{(\alpha U_f \ell) U_{2D}^2}{L^2} - \frac{(\gamma U_{3D} H) U_f^2}{\ell^2}, \tag{A 1b}$$

$$\partial_t U_{3D}^2 = \frac{(\beta U_{3D} H) U_{2D}^2}{L^2} + \frac{(\gamma U_{3D} H) U_f^2}{\ell^2} - \frac{U_{3D}^3}{H}. \tag{A 1c}$$

One can easily see that these equations do not permit a fixed point with $U_{3D} = 0$ when $\epsilon \neq 0$. To show this, first note that, as in the finite Re case, the forcing-scale velocity U_f cannot vanish at a fixed point if $\epsilon \neq 0$. Assume there exists a fixed point with $U_{3D} = 0$. Then equation (A 1c) is trivially satisfied, while (A 1a) implies that $U_{2D} = 0$ or $U_f = 0$. Since U_f must be non-zero, we have $U_{2D} = 0$, which leads to a contradiction in equation (A 1b) for any $\epsilon \neq 0$. Hence neither a laminar flow state nor a 2-D condensate state exists in the system in the infinite Re limit. The only two remaining fixed points are 3-D turbulence and the flux-loop condensate. The former is given by

$$U_{2D}^2 = 0, \quad U_f^2 = \frac{\epsilon^{2/3} \ell^2}{\gamma H^{4/3}}, \quad U_{3D}^2 = (\epsilon H)^{2/3}. \tag{A 2a-c}$$

Using this result and considering equation (A 1a), we can find that the 3-D turbulence fixed point becomes unstable to 2-D perturbations at

$$H = \left(\frac{\alpha^2}{\beta^2 \gamma} \right)^{1/4} \ell \tag{A 3}$$

and thus we obtain that

$$Q_{3D} = \left(\frac{\beta^2 \gamma}{\alpha^2} \right)^{1/4}. \tag{A 4}$$

Hence, in the low viscosity limit of our three-scale model, there remains only one bifurcation, namely that at Q_{3D} between two-dimensional turbulence and the split cascade state. The second critical point Q_{2D} vanishes to infinity as $Q_{2D} \propto Re^{3/4}$ in this limit. Figure 20 demonstrates close to Q_{3D} that the full model converges to the solution obtained from the asymptotic form of the equations (A 1) as Re increases. This is consistent with the convergence observed in the DNS in figure 6(b).

At finite viscosity, one has to solve the full equations, (6.5) which is difficult analytically for the 2-D condensate state. In order to facilitate analytical progress in deriving predictions from the model, one may formally take the high viscosity limit in which the different eddy viscosities take the form of equation (6.2). The model equations then become

$$\partial_t U_{2D}^2 = - \left(\nu - \alpha \frac{U_f^2 \ell^2}{\nu} + \beta \frac{U_{3D}^2 H^2}{\nu} \right) \frac{U_{2D}^2}{L^2}, \tag{A 5a}$$

$$\partial_t U_f^2 = \epsilon - \left(\nu + \gamma \frac{U_{3D}^2 H^2}{\nu} \right) \frac{U_f^2}{\ell^2} - \alpha \frac{U_f^2 \ell^2}{\nu} \frac{U_{2D}^2}{L^2}, \tag{A 5b}$$

$$\partial_t U_{3D}^2 = \beta \frac{U_{3D}^2 H^2}{\nu} \frac{U_{2D}^2}{L^2} + \gamma \frac{U_{3D}^2 H^2}{\nu} \frac{U_f^2}{\ell^2} - \frac{U_{3D}^3}{H} - \nu \frac{U_{3D}^2}{H^2}. \tag{A 5c}$$

To obtain this limiting form of the equations, it is assumed that $\nu \gg U_f \ell, U_{3D} H$, while no restriction is imposed on U_{2D} ; in particular, the case of a large-scale-based Reynolds number in the large scales $U_{2D} L / \nu$, which is most relevant in the condensate state, is included. The laminar flow is unstable to 3-D perturbations when $Q < \gamma^{1/4} Re^{3/4}$ and unstable to 2-D perturbations when

$$Re > 1/\alpha^{1/3}. \tag{A 6}$$

When the latter condition is satisfied and H is sufficiently small (Q sufficiently large), the system is attracted to the 2-D condensate state, given by

$$U_{2D}^2 = \frac{L^2}{\nu} \left(\epsilon - \frac{\nu^3}{\ell^4 \alpha} \right), \quad U_f^2 = \frac{\nu^2}{\alpha \ell^2}, \quad U_{3D} = 0. \tag{A 7a-c}$$

Note that U_{2D}^2 is inversely proportional to the viscosity and proportional to L^2 in agreement with the scaling of the data in figure 6(b). The 2-D condensate state ceases to be an attractor of the system when H is sufficiently large such that U_{3D} becomes unstable. This occurs when

$$H^4 > \left(\beta \frac{\epsilon}{\nu^3} + \frac{\gamma - \beta}{\alpha \ell^4} \right)^{-1}. \tag{A 8}$$

Hence, we conclude that

$$Q_{2D} = \left(\beta \frac{\epsilon \ell^4}{\nu^3} + \frac{\gamma - \beta}{\alpha} \right)^{1/4} = \left(\beta Re^3 + \frac{\gamma - \beta}{\alpha} \right)^{1/4}. \tag{A 9}$$

Thus, for moderate values of Re , there is an approximate scaling $Q_{2D} \propto Re^{3/4} \propto \eta$, the dissipation length (note that $Re^3 > 1/\alpha$ due to (A 6)), in agreement with the results obtained in § 3, where we showed that the U_{2D}^2 data points collapse under rescaling such that $Q Re^{3/4} = \eta/H$ is on the abscissa and $U_{2D}^2 K^2 / [Re(\epsilon \ell)^{2/3}]$ on the coordinate. Results from the full model equations (6.3) and (6.5) are shown in figure 21 where the same scaling is applied. The corresponding plots for equations (A 5) are very similar. Furthermore, an asymptotic analysis close to Q_{2D} described in § A.2 of this appendix reveals that the scaling for $U_{3D}^2 \propto (Q_{2D} - Q)^2$ which is the same as in the DNS results shown in figure 8(b) although no intermittency is present. The other critical point Q_{3D} , where the 3-D turbulence solution changes stability, can be evaluated numerically and is found to increase with Re indefinitely. This, however, is an artefact of the high viscosity asymptotic form of the eddy viscosities used in this subsection.

A.2. Behaviour of U_{3D} near Q_{2D}

Here, we derive the behaviour close to H_{2D} in the three-scale model. First consider $H = H_{2D}(1 + \delta)$ and let $\mathbf{x} = (x, y, z)^T = (U_{2D}^2, U_f^2, U_{3D}^2)^T$, $\tilde{\mathbf{x}} = (\tilde{x}, \tilde{y}, \tilde{z})^T = \mathbf{x} - (x_{2D}, y_{2D}, 0)^T$,

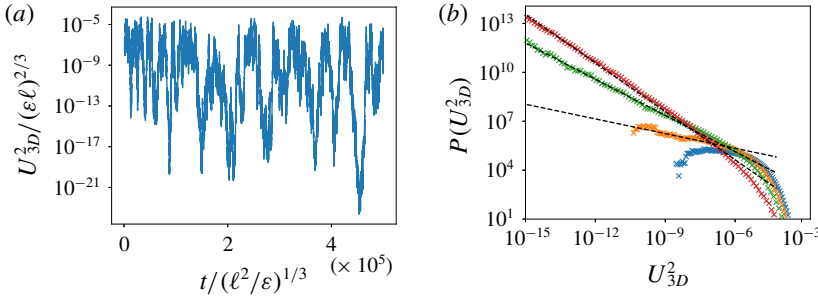


FIGURE 22. (Colour online) Time series and PDF showing on–off intermittency close to $Q_{2D} \approx 1.638$ in the three-scale model with a fluctuating energy injection rate. Parameters: (a) $Q = 1.63775$, $L = 10\ell$, $Re = 2$, $\alpha = 0.001$, $\beta = 10$, $\gamma = 0.9$, $\sigma = 0.1$, (b) $q = 1.635, 1.636, 1.637, 1.63775$ (bottom to top), other parameters identical. Dashed lines in (b) are power laws with exponents $-0.3 -0.74, -0.99$ (bottom to top): cf. figures 12 and 8(b).

where x_{2D} and y_{2D} are the values of U_{2D}^2 and U_f^2 respectively at $H = H_{2D}$. Then equations (A 5) can be rewritten exactly in the form

$$\frac{d}{dt} \tilde{\mathbf{x}} = \begin{pmatrix} -\frac{\nu}{L^2} & \frac{\alpha \ell^2 x_2}{\nu L^2} & -\frac{\beta x_2 H^2}{\nu L^2} \\ -\frac{\alpha y_2}{\nu L^2} & \frac{\nu}{\ell^2} & -\frac{\gamma H^2 y_2}{\nu \ell^2} \\ 0 & 0 & C \end{pmatrix} \tilde{\mathbf{x}} + \begin{pmatrix} 0 \\ 0 \\ -1/H_{2D} \end{pmatrix} \tilde{z}^{3/2} + \tilde{\mathbf{x}}^T \mathbf{B} \tilde{\mathbf{x}}, \quad (\text{A } 10)$$

where $C = -\nu/H^2 + \beta H^2 x_2/\nu L^2 + \gamma H^2 y_2/\nu \ell^2$ and the specific coefficients of the quadratic term are irrelevant here. By definition of H_{2D} , $C(\delta = 0) = -\nu/H_{2D}^2 + \beta H_{2D}^2 x_2/\nu L^2 + \gamma H_{2D}^2 y_2/\nu \ell^2 = 0$. Hence, for small δ , $C \propto \delta$. Specifically,

$$C \stackrel{\delta \ll 1}{\approx} \left(\frac{2\nu}{H_{2D}^2} + \frac{2\beta x_2}{\nu L^2} + \frac{2\gamma y_2}{\nu \ell^2} \right) \delta. \quad (\text{A } 11)$$

Hence, considering the \tilde{z} component and balancing the linear term with the $\tilde{z}^{3/2}$ term, we deduce that

$$\tilde{z} \stackrel{\delta \ll 1}{\approx} \left(\frac{2\nu}{H_{2D}^2} + \frac{2\beta x_2 H_{2D}^2}{\nu L^2} + \frac{2\gamma y_2 H_{2D}^2}{\nu \ell^2} \right)^2 H_{2D}^2 \delta^2. \quad (\text{A } 12)$$

This means that $U_{3D}^2 \propto \delta^2$, which is precisely the scaling observed in figure 8(b). It is important to note however that the asymptotic result (A 12) is only valid for very small δ and cannot be extended to $\delta \sim O(1)$ where the quadratic terms are dominant.

A.3. On–off intermittency in the three-scale model

When a fluctuating energy injection rate is taken into account in the model by replacing $\epsilon \rightarrow \epsilon + \sigma \zeta$, where $\zeta \sim \mathcal{N}(0, 1)$ is Gaussian white noise, on–off intermittency in U_{3D}^2 can be observed in the three-scale model. This is illustrated in figure 22 in

terms of the time series of U_{3D}^2 and the corresponding PDF, which approaches a power law with exponent -1 as $Q \rightarrow Q_{2D}$.

REFERENCES

- ALEXAKIS, A. 2011 Two-dimensional behavior of three-dimensional magnetohydrodynamic flow with a strong guiding field. *Phys. Rev. E* **84** (5), 056330.
- ALEXAKIS, A. 2015 Rotating Taylor–Green flow. *J. Fluid Mech.* **769**, 46–78.
- ALEXAKIS, A. 2018 Three-dimensional instabilities and negative eddy viscosity in thin-layer flows. *Phys. Rev. Fluids* **3**, 114601.
- ALEXAKIS, A. & BIFERALE, L. 2018 Cascades and transitions in turbulent flows. *Phys. Rep.* **767–769**, 1–101.
- BARTELLO, P., MÉTAIS, O. & LESIEUR, M. 1994 Coherent structures in rotating three-dimensional turbulence. *J. Fluid Mech.* **273**, 1–29.
- BAYLY, B. J. & YAKHOT, V. 1986 Positive-and negative-effective-viscosity phenomena in isotropic and anisotropic beltrami flows. *Phys. Rev. A* **34** (1), 381.
- BENAVIDES, S. & ALEXAKIS, A. 2017 Critical transitions in thin layer turbulence. *J. Fluid Mech.* **822**, 364–385.
- BOFFETTA, G. & ECKE, R. E. 2012 Two-dimensional turbulence. *Annu. Rev. Fluid Mech.* **44** (1), 427–451.
- BOUCHET, F. & SIMONNET, E. 2009 Random changes of flow topology in two-dimensional and geophysical turbulence. *Phys. Rev. Lett.* **102** (9), 094504.
- BOUSSINESQ, J. 1877 *Essai sur la Théorie des Eaux Courantes*. Impr. Nationale.
- BYRNE, D., XIA, H. & SHATS, M. G. 2011 Robust inverse energy cascade and turbulence structure in three-dimensional layers of fluid. *Phys. Fluids* **23** (9), 095109.
- CAMERON, A., ALEXAKIS, A. & BRACHET, M.-E. 2016 Large-scale instabilities of helical flows. *Phys. Rev. Fluids* **1** (6), 063601.
- CAMERON, A., ALEXAKIS, A. & BRACHET, M.-E. 2017 Effect of helicity on the correlation time of large scales in turbulent flows. *Phys. Rev. Fluids* **2** (11), 114602.
- CELANI, A., MUSACCHIO, S. & VINCENZI, D. 2010 Turbulence in more than two and less than three dimensions. *Phys. Rev. Lett.* **104**, 184506.
- CHAN, C.-K., MITRA, D. & BRANDENBURG, A. 2012 Dynamics of saturated energy condensation in two-dimensional turbulence. *Phys. Rev. E* **85**, 036315.
- CHERTKOV, M., CONNAUGHTON, C., KOLOKOLOV, I. & LEBEDEV, V. 2007 Dynamics of energy condensation in two-dimensional turbulence. *Phys. Rev. Lett.* **99** (8), 084501.
- DALLAS, V., FAUVE, S. & ALEXAKIS, A. 2015 Statistical equilibria of large scales in dissipative hydrodynamic turbulence. *Phys. Rev. Lett.* **115** (20), 204501.
- DARRIGOL, O. 2017 Joseph boussinesq’s legacy in fluid mechanics. *C. R. Méc.* **345** (7), 427–445.
- DEUSEBIO, E., BOFFETTA, G., LINDBORG, E. & MUSACCHIO, S. 2014 Dimensional transition in rotating turbulence. *Phys. Rev. E* **90** (2), 023005.
- DUBRULLE, B. & FRISCH, U. 1991 Eddy viscosity of parity-invariant flow. *Phys. Rev. A* **43**, 5355–5364.
- FAVIER, B., GUERVILLY, C. & KNOBLOCH, E. 2019 Subcritical turbulent condensate in rapidly rotating Rayleigh–Bénard convection, *J. Fluid Mech.* (in press) Preprint, [arXiv:1901.04269](https://arxiv.org/abs/1901.04269).
- FAVIER, B., SILVERS, L. J. & PROCTOR, M. R. E. 2014 Inverse cascade and symmetry breaking in rapidly rotating boussinesq convection. *Phys. Fluids* **26** (9), 096605.
- FRISCH, U. 1995 *Turbulence: The Legacy of AN Kolmogorov*. Cambridge University Press.
- FRISHMAN, A. & HERBERT, C. 2018 Turbulence statistics in a two-dimensional vortex condensate. *Phys. Rev. Lett.* **120**, 204505.
- FRISHMAN, A., LAURIE, J. & FALKOVICH, G. 2017 Jets or vortices what flows are generated by an inverse turbulent cascade? *Phys. Rev. Fluids* **2** (3), 032602.
- FUJISAKA, H. & YAMADA, T. 1985 A new intermittency in coupled dynamical systems. *Prog. Theor. Phys.* **74** (4), 918–921.

- GALLET, B. & DOERING, C. R. 2015 Exact two-dimensionalization of low-magnetic-Reynolds-number flows subject to a strong magnetic field. *J. Fluid Mech.* **773**, 154–177.
- GAMA, S., VERGASSOLA, M. & FRISCH, U. 1994 Negative eddy viscosity in isotropically forced two-dimensional flow: linear and nonlinear dynamics. *J. Fluid Mech.* **260**, 95–126.
- GUERVILLY, C., HUGHES, D. W. & JONES, C. A. 2014 Large-scale vortices in rapidly rotating Rayleigh–Bénard convection. *J. Fluid Mech.* **758**, 407–435.
- HEFER, D. & YAKHOT, V. 1989 Inverse energy cascade in a time dependent flow. *Phys. Fluids A* **1** (8), 1383–1386.
- HOSSAIN, M., MATTHAEUS, W. H. & MONTGOMERY, D. 1983 Long-time states of inverse cascades in the presence of a maximum length scale. *J. Plasma Phys.* **30** (3), 479–493.
- KRAICHNAN, R. H. 1967 Inertial ranges in two-dimensional turbulence. *Phys. Fluids* **10** (7), 1417–1423.
- KRAICHNAN, R. H. 1973 Helical turbulence and absolute equilibrium. *J. Fluid Mech.* **59** (4), 745–752.
- KRAICHNAN, R. H. 1976 Eddy viscosity in two and three dimensions. *J. Atmos. Sci.* **33** (8), 1521–1536.
- KUKHARKIN, N. & ORSZAG, S. A. 1996 Generation and structure of Rossby vortices in rotating fluids. *Phys. Rev. E* **54**, R4524–R4527.
- KUKHARKIN, N., ORSZAG, S. A. & YAKHOT, V. 1995 Quasicrystallization of vortices in drift-wave turbulence. *Phys. Rev. Lett.* **75** (13), 2486.
- LE DÉZ, S. & LAPORTE, F. 2002 Theoretical predictions for the elliptical instability in a two-vortex flow. *J. Fluid Mech.* **471**, 169–201.
- MARINO, R., POUQUET, A. & ROSENBERG, D. 2015 Resolving the paradox of oceanic large-scale balance and small-scale mixing. *Phys. Rev. Lett.* **114** (11), 114504.
- MESHALKIN, L. D. 1962 Investigation of the stability of a stationary solution of a system of equations for the plane movement of an incompressible viscous liquid. *Z. Angew. Math. Mech. J. Appl. Math. Mech.* **25**, 1700–1705.
- MININNI, P. D., ROSENBERG, D., REDDY, R. & POUQUET, A. 2011 A hybrid mpi–openmp scheme for scalable parallel pseudospectral computations for fluid turbulence. *Parallel Comput.* **37** (6–7), 316–326.
- MUSACCHIO, S. & BOFFETTA, G. 2017 Split energy cascade in turbulent thin fluid layers. *Phys. Fluids* **29** (11), 111106.
- PARET, J. & TABELING, P. 1997 Experimental observation of the two-dimensional inverse energy cascade. *Phys. Rev. Lett.* **79** (21), 4162.
- PARET, J. & TABELING, P. 1998 Intermittency in the two-dimensional inverse cascade of energy: Experimental observations. *Phys. Fluids* **10** (12), 3126–3136.
- PEDLOSKY, J. 2013 *Geophysical Fluid Dynamics*. Springer.
- PLATT, N., SPIEGEL, E. A. & TRESSER, C. 1993 On-off intermittency: A mechanism for bursting. *Phys. Rev. Lett.* **70**, 279–282.
- RAVELET, F., MARIÉ, L., CHIFFAUDEL, A. & DAVIAUD, F. 2004 Multistability and memory effect in a highly turbulent flow: experimental evidence for a global bifurcation. *Phys. Rev. Lett.* **93**, 164501.
- RUBIO, A. M., JULIEN, K., KNOBLOCH, E. & WEISS, J. B. 2014 Upscale energy transfer in three-dimensional rapidly rotating turbulent convection. *Phys. Rev. Lett.* **112** (14), 144501.
- SAHOO, G., ALEXAKIS, A. & BIFERALE, L. 2017 Discontinuous transition from direct to inverse cascade in three-dimensional turbulence. *Phys. Rev. Lett.* **118** (16), 164501.
- SAHOO, G. & BIFERALE, L. 2015 Disentangling the triadic interactions in Navier–Stokes equations. *Eur. Phys. J. E* **38** (10), 114.
- DE SAINT-VENANT, B. 1843 Notea jointre au mémoire sur la dynamique des fluides. *Comptes Rendus* **17**, 1240–1244.
- SESHASAYANAN, K. & ALEXAKIS, A. 2016 Critical behavior in the inverse to forward energy transition in two-dimensional magnetohydrodynamic flow. *Phys. Rev. E* **93** (1), 013104.
- SESHASAYANAN, K. & ALEXAKIS, A. 2018 Condensates in rotating turbulent flows. *J. Fluid Mech.* **841**, 434–462.

- SESHASAYANAN, K., BENAVIDES, S. J. & ALEXAKIS, A. 2014 On the edge of an inverse cascade. *Phys. Rev. E* **90** (5), 051003.
- SHATS, M. G., XIA, H. & PUNZMANN, H. 2005 Spectral condensation of turbulence in plasmas and fluids and its role in low-to-high phase transitions in toroidal plasma. *Phys. Rev. E* **71** (4), 046409.
- SHATS, M. G., XIA, H., PUNZMANN, H. & FALKOVICH, G. 2007 Suppression of turbulence by self-generated and imposed mean flows. *Phys. Rev. Lett.* **99** (16), 164502.
- SIVASHINSKY, G. & YAKHOT, V. 1985 Negative viscosity effect in large-scale flows. *Phys. Fluids* **28** (4), 1040–1042.
- SMITH, L. M., CHASNOV, J. R. & WALEFFE, F. 1996 Crossover from two-to three-dimensional turbulence. *Phys. Rev. Lett.* **77** (12), 2467.
- SMITH, L. M. & YAKHOT, V. 1993 Bose condensation and small-scale structure generation in a random force driven 2d turbulence. *Phys. Rev. Lett.* **71** (3), 352.
- SMITH, L. M. & YAKHOT, V. 1994 Finite-size effects in forced two-dimensional turbulence. *J. Fluid Mech.* **274**, 115–138.
- SOMMERIA, J. 1986 Experimental study of the two-dimensional inverse energy cascade in a square box. *J. Fluid Mech.* **170**, 139–168.
- SOZZA, A., BOFFETTA, G., MURATORE-GINANNESCHI, P. & MUSACCHIO, S. 2015 Dimensional transition of energy cascades in stably stratified forced thin fluid layers. *Phys. Fluids* **27** (3), 035112.
- TAYLOR, G. I. 1915 I. eddy motion in the atmosphere. *Phil. Trans. R. Soc. Lond. A* **215** (523–537), 1–26.
- TAYLOR, G. I. 1922 Diffusion by continuous movements. *Proc. R. Soc. Lond.* **2** (1), 196–212.
- VALLIS, G. K. & MALTRUD, M. E. 1993 Generation of mean flows and jets on a beta plane and over topography. *J. Phys. Oceanogr.* **23** (7), 1346–1362.
- VENAILLE, A. & BOUCHET, F. 2011 Oceanic rings and jets as statistical equilibrium states. *J. Phys. Oceanogr.* **41** (10), 1860–1873.
- WEEKS, E. R., TIAN, Y. D., URBACH, J. S., IDE, K., SWINNEY, H. L. & GHIL, M. 1997 Transitions between blocked and zonal flows in a rotating annulus with topography. *Science* **278** (5343), 1598–1601.
- XIA, H., BYRNE, D., FALKOVICH, G. & SHATS, M. G. 2011 Upscale energy transfer in thick turbulent fluid layers. *Nat. Phys.* **7** (4), 321.
- XIA, H. & FRANCOIS, N. 2017 Two-dimensional turbulence in three-dimensional flows. *Phys. Fluids* **29** (11), 111107.
- XIA, H., PUNZMANN, H., FALKOVICH, G. & SHATS, M. G. 2008 Turbulence-condensate interaction in two dimensions. *Phys. Rev. Lett.* **101** (19), 194504.
- XIA, H., SHATS, M. G. & FALKOVICH, G. 2009 Spectrally condensed turbulence in thin layers. *Phys. Fluids* **21** (12), 125101.
- YAKHOT, V. & SIVASHINSKY, G. 1987 Negative-viscosity phenomena in three-dimensional flows. *Phys. Rev. A* **35**, 815–820.
- YOKOYAMA, N. & TAKAOKA, M. 2017 Hysteretic transitions between quasi-two-dimensional flow and three-dimensional flow in forced rotating turbulence. *Phys. Rev. Fluids* **2** (9), 092602.